OBSERVATIONS OF THE 10 MAY 2010 TORNADO OUTBREAK USING OU-PRIME

Potential for New Science with High-Resolution Polarimetric Radar

BY ROBERT D. PALMER, DAVID BODINE, MATTHEW KUMJIAN, BOONLENG CHEONG, GUIFU ZHANG, QING CAO, HOWARD B. BLUESTEIN, ALEXANDER RYZHKOV, TIAN-YOU YU, AND YADONG WANG

New high-resolution polarimetric radar reveals detailed storm structure.

Since the early 1970s, Doppler radar has been used as the primary tool in advancing our knowledge of the kinematics and dynamics of severe convective storms. In particular, a pair of fixed-site, S-band Doppler radars in central Oklahoma was used by the National Severe Storms Laboratory (NSSL) in Norman for a number of years. Based on single- and dual-Doppler data collected by the serendipitous nearby passage of tornadic supercells, much was learned about supercell structure, dynamics, and tornado formation (e.g., Brandes 1984). Alas, the number of cases available was limited by the relatively few storms caught in the act of producing tornadoes within the small area for which dual-Doppler observations were available (within ~80 km of each radar). For example, between 1970 and 2010, the best cases documented in the literature of tornadic storms near fixed-site radars in central Oklahoma total only about 10 in the 40-yr period (Lemon et al. 1978; Brandes 1984; Zrnić et al. 1985; MacGorman et al. 1989; Dowell and Bluestein 1997; Burgess et al. 2002; Hu and Xue 2007; Romine et al. 2008). Furthermore, it is extremely unlikely and rare for a tornado to form close enough to one of the radars (within ~5–10 km) so that tornado-scale measurements could be made.

AFFILIATIONS: PALMER, BODINE, AND ZHANG—School of Meteorology, and Atmospheric Radar Research Center, University of Oklahoma, Norman, Oklahoma; KUMJIAN, RYZHKOV, AND WANG—Cooperative Institute for Mesoscale Meteorological Studies, University of Oklahoma, Norman, Oklahoma; CHEONG AND CAO—Atmospheric Radar Research Center, University of Oklahoma, Norman, Oklahoma; BLUESTEIN—School of Meteorology, University of Oklahoma, Norman, Oklahoma; YU—School of Electrical and Computer Engineering, and Atmospheric Radar Research Center, University of Oklahoma, Norman, Oklahoma

CORRESPONDING AUTHOR: Robert D. Palmer, Atmospheric Radar Research Center, University of Oklahoma, 120 David L. Boren Blvd., Suite 4610, Norman, OK 73072
E-mail: rpalmer@ou.edu

The abstract for this article can be found in this issue, following the table of contents.

DOI:10.1175/2011BAMS3125.1

In final form 24 February 2011
©2011 American Meteorological Society

To increase the likelihood of obtaining close observations of supercells and tornadoes, airborne X-band Doppler radars were designed (e.g., Wakimoto et al. 1996) and ground-based, mobile Doppler radars operating at W, X, and C bands were designed and mounted on vans and trucks as platforms (e.g., Bluestein and Unruh 1989; Bluestein et al. 1995; Wurman et al. 1997; Wurman and Randall 2001; Biggerstaff et al. 2005; Bluestein et al. 2007, 2010). Such mobile platforms could provide storm-scale observations and, when close to the target storm, substorm-scale and tornado-scale observations. Shorter radar wavelengths are chosen for practical reasons (e.g., antenna size), providing finescale observations at close but safe ranges. However, X- and W-band radar data are inhibited by attenuation in heavy precipitation, whereas S- and C-band measurements are less affected.

Until recently, the information collected by radars has been limited to precipitation intensity and velocity. Since the idea of measuring differential reflectivity Z_{DR} was first proposed by Seliga and Bringi (1976), the advent of dual-polarization weather radars has led to numerous advancements (Herzegh and Jameson 1992; Zrnić 1996; Zrnić and Ryzhkov 1999; Bringi and Chandrasekar 2001). Weather radar polarimetry has now become a mature and desirable technology for both fixed (Doviak et al. 2000) and mobile (e.g., Bluestein et al. 2007) radars. In addition to radar reflectivity Z_H, Doppler velocity v_r, and spectrum width σ_v, dual-polarization radars are capable of measuring the differential reflectivity Z_{DR}, differential propagation phase Φ_{DP} and the specific differential phase K_{DP}, and the copolar cross-correlation coefficient ρ_{hv}. This additional information provided by polarimetric radar has great potential in elucidating precipitation physics, including hydrometeor classification (Vivekanandan et al. 1999; Zrnić and Ryzhkov 1999; Straka et al. 2000; Park et al. 2009; Snyder et al. 2010), accurate quantitative precipitation estimation (Brandes et al. 2002; Ryzhkov et al. 2005a,b; Giangrande and Ryzhkov 2008), and retrieval of particle size distributions (Zhang et al. 2001; Bringi et al. 2002) in various precipitating systems.

In particular, supercell storms have been an active area of research using dual-polarization radars (e.g., Conway and Zrnić 1993; Hubbert et al. 1998; Loney et al. 2002; Ryzhkov et al. 2005c; Kumjian and Ryzhkov 2008; Romine et al. 2008; Payne et al. 2010; Kumjian et al. 2010) because of their substantial impacts on society and the inherent dangers of in situ measurements in such storms. Kumjian and Ryzhkov (2008) found repetitive signatures characteristic of supercells, including Z_{DR} and K_{DP} columns, the low-level Z_{DR} arc and signature of large hail, midlevel Z_{DR} and ρ_{hv} rings, and the tornadic debris signature. These signatures not only illuminate certain microphysical processes but also reveal unique links to kinematic features of storms, such as updrafts, downdrafts, mesocyclones, damaging tornadoes, and environmental storm-relative helicity (Kumjian and Ryzhkov 2009).

In 2003, the University of Oklahoma (OU) decided to build on the strong foundation of weather radar research in Norman by investing specifically in 10 new faculty positions, support staff, and experimental infrastructure. This Strategic Radar Initiative emphasized both the meteorological and engineering aspects of weather radar, enhanced the partnership between OU and the National Oceanic and Atmospheric Administration (NOAA), and created new relationships with the private sector. Out of this initiative grew the Atmospheric Radar Research Center (ARRC), which embodies the interdisciplinary nature of the field. A comprehensive educational program in weather radar also emerged from this initiative by leveraging a grassroots effort by the weather radar faculty (Palmer et al. 2009). With the Strategic Radar Initiative as the backdrop and with the emerging importance of polarimetric radar, it quickly became apparent that a high-quality polarimetric radar, focused on the educational and research missions of the university, was needed. In partnership with Enterprise Electronics Corporation (EEC), OU embarked on the development of the OU Polarimetric Radar for Innovations in Meteorology and Engineering (OU-PRIME) facility, which was commissioned on 4 April 2009. Initial work with OU-PRIME has focused on comparative, multiple-wavelength studies exploiting other independent radars in Norman (e.g., Picca and Ryzhkov 2010; Borowska et al. 2011; Gu et al. 2011) and the development and implementation of advanced signal processing algorithms (Wang et al. 2008; Lei et al. 2009; Warde and Torres 2010).

On 10 May 2010, OU-PRIME was operated by the ARRC in a sector-scanning mode to provide relatively rapid volumetric updates (2–3 min). Data collection spanned 1400–2331 UTC, with several tornadoes observed near the radar site between 2220 and 2331 UTC. With the radar's intrinsic 0.45° beamwidth and high sensitivity and the close proximity of the tornadoes, the resulting dataset holds promise to provide a wealth of new information about tornadogenesis, supercell structure and microphysics, and storm interactions, in addition to the development and assessment of signal processing algorithms (e.g., tornado detection) based on polarimetric data. In this article, a brief summary of the 10 May 2010 tornado

outbreak will be provided. A technical description of the OU-PRIME radar, performance/sensitivity comparisons, and resolution characteristics will be discussed. Finally, examples of the high-resolution polarimetric data will be provided along with several proposed avenues for future research and possibilities for collaboration.

ENVIRONMENTAL CONDITIONS LEADING TO OUTBREAK. On 10 May 2010, 55 tornadoes in five or more supercells struck parts of north-central, central, south-central, and eastern Oklahoma. Of these, the strongest two were rated enhanced Fujita scale ratings of 4 (EF-4; www.depts.ttu.edu/weweb/F_scale/images/efsr.pdf) and both of these occurred in or near Norman (Fig. 1). Three people were killed and considerable damage was reported with these tornadoes (Fig. 1: Lake Thunderbird and Little Axe photos); more than 100 homes were destroyed. This was the largest tornado outbreak in Oklahoma since 3 May 1999, when 62 tornadoes were documented in 10 supercells (Speheger et al. 2002).

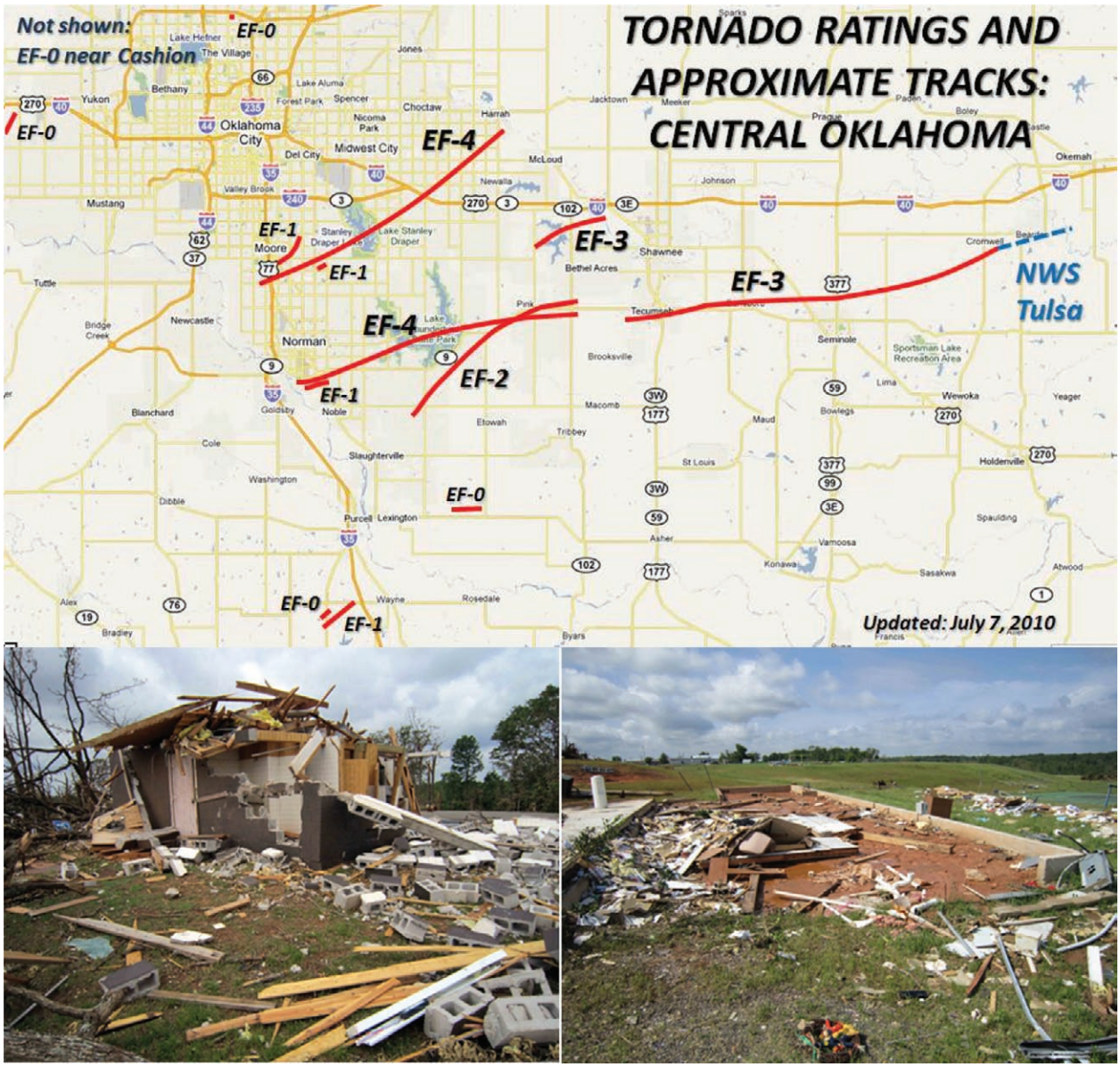

Fig. 1. (top) Tornado tracks on 10 May 2010 in central Oklahoma along with the EF ratings of the tornadoes (courtesy of the Norman NWS office). Photographs of damage inflicted by the EF-4 tornado that struck Norman, OK, on 10 May 2010: (bottom left) damage at a campsite at Lake Thunderbird State Park and (bottom right) school building wiped clear of its foundation at Little Axe, just east of Lake Thunderbird (courtesy of H. Bluestein).

Because the tornado outbreak occurred during the second year of a major field experiment, the Verification of the Origin of Rotation in Tornadoes Experiment 2 (VORTEX2; www.vortex2.org/home/), there was both a heightened awareness of the environmental conditions and an increase in the number of observational facilities. One of the authors provided nowcast support for OU-PRIME from the VORTEX2 operations center during the tornado outbreak, utilizing additional high-resolution model runs and observations from the field, such as mobile soundings or mobile Mesonet observations (e.g., Straka et al. 1996). Early on the morning of 10 May 2010, a "high risk" of severe weather was forecast for a portion of northern, northeastern, and central Oklahoma, the highest probability category issued by the Storm Prediction Center (SPC). By afternoon, there was relatively high convective available potential energy (CAPE) and relatively strong vertical shear in central Oklahoma, necessary conditions for the formation of supercells (Weisman and Klemp 1982; Rasmussen and Blanchard 1998; Rasmussen 2003). A special sounding released at Norman just a few hours before storms impacted the Norman area was characterized by a most unstable CAPE (MUCAPE) in excess of 3000 J kg^{-1} and surface to 6-km wind magnitude difference of 35–40 m s^{-1} (Fig. 2). In addition, storm-relative helicity in excess of 300 and 400 m^2 s^{-2} in the lowest 1 and 3 km, respectively, and a lifting condensation level (LCL) of less than 700 m were indicated. These parameters are among the extreme values seen in nature and in numerical forecast models when there are tornadic supercells (Rasmussen and Blanchard 1998; Rasmussen 2003; Thompson et al. 2003, 2007).

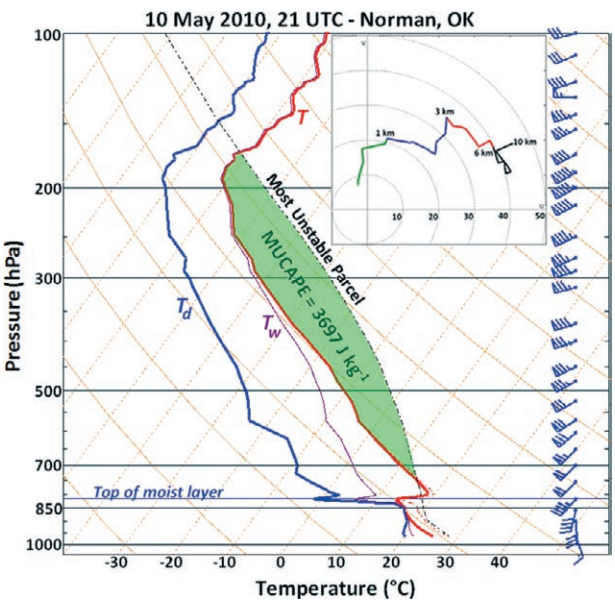

Fig. 2. Special sounding released by the NWS in Norman for 2100 UTC 10 May 2010. Thermodynamic sounding (temperature *T* in °C is shown in red; dewpoint temperature T_d in °C is shown in blue; wet-bulb temperature T_w is shown in purple; pressure in hPa is shown to the left; and flags, wind barbs, and half wind barbs denote 50, 10, and 5 kt, respectively); the top-right inset shows a hodograph, with winds plotted in m s^{-1} and heights shown in km. Colors on the hodograph represent the layers 0–1 (green), 1–3 (blue), 3–6 (red), and 6–10 km (black).

In addition to the necessary environmental conditions for tornadic supercells, the conditions in the synoptic and mesoscale environment also favored storm initiation. Convective inhibition (CIN) for the 2100 UTC Norman sounding (Fig. 2) was ~30–60 J kg^{-1}, suggesting that strong upward motion was necessary to initiate deep convection or that CIN was locally much weaker because of small-scale thermodynamic variability (e.g., Bodine et al. 2010). An intense synoptic-scale upstream trough approaching from the west (e.g., at 500 hPa in Fig. 3a) provided synoptic-scale ascent in the lower and middle troposphere (Fig. 3b). The strongest upward motion focused on eastern Kansas, but some weaker yet substantial upward motion extended southward through central and eastern Oklahoma. The trough acted to increase the vertical shear as it approached central Oklahoma, whereas mesoscale, low-level lifting along a strongly convergent dryline (Fig. 4) was apparently sufficient to initiate storms, which then propagated away from the dryline (Fig. 5).

Convective storms formed first in northwestern Oklahoma (Fig. 5a) and then later southward into central and south-central Oklahoma (Fig. 5b). They then assumed the orientation of a broken line of cells across central Oklahoma (Fig. 5c), while convection redeveloped along the dryline to the west (Fig. 5d) and some neighboring cells interacted with each other. Figure 5c shows reflectivity images of the supercells in Norman and Moore near the time when they were producing tornadoes.

DESCRIPTION OF OU-PRIME. *Technical specifications.* Working closely with OU-ARRC researchers on its specification and design, EEC built and installed OU-PRIME during the latter part of 2008 and early 2009 near the National Weather Center (NWC) building on OU's research campus. A sequence of photographs during construction (radome installation) is provided in Fig. 6. System specifications of OU-PRIME are given in Table 1 along with a comparison to the nascent polarimetric version of the Weather Surveillance Radar-1988 Doppler (WSR-88D).

During the design phase of OU-PRIME, OU-ARRC researchers decided that a high-resolution, C-band, polarimetric radar system had the potential to reveal new science and create opportunities for the university community. A high-resolution, C-band, polarimetric radar offered higher spatial resolution than the polarimetric version of the WSR-88D (Table 1), providing an opportunity to examine finer-scale features of different phenomena. Therefore, one of the major design decisions was to build a radar with a 0.45° intrinsic beamwidth, which requires an 8.5-m dish (same size as the WSR-88D radars) at the C-band frequency of 5510 MHz. The OU-PRIME dish is a commercially available design for polarimetric applications with a first sidelobe level of –27 dB, cross-polar isolation of at least –35 dB, and a gain of 50 dB. Of course, it is well known that a drawback of the chosen C-band wavelength is attenuation and differential attenuation (e.g., Tabary et al. 2009). Given that OU-PRIME is a research radar, however, this fact was viewed as an opportunity for algorithm development related to attenuation correction based on polarimetric data (Bringi et al. 1990, 2001; Carey et al. 2000; Testud et al. 2000; Gourley et al. 2007; Vulpiani et al. 2008).

OU-PRIME has a 1-MW magnetron transmitter and uses a simultaneous transmit–simultaneous receive (STSR) configuration, which is being used for the national WSR-88D network. This decision was made in part because of the inherent advantages of the STSR mode (e.g., Doviak et al. 2000), notably the compatibility with the current operational WSR-88D algorithms and the simplicity of the required hardware upgrade. However, a drawback of radars operating in the STSR mode is possible cross-polar contamination, which can lead to errors in Z_{DR} as a

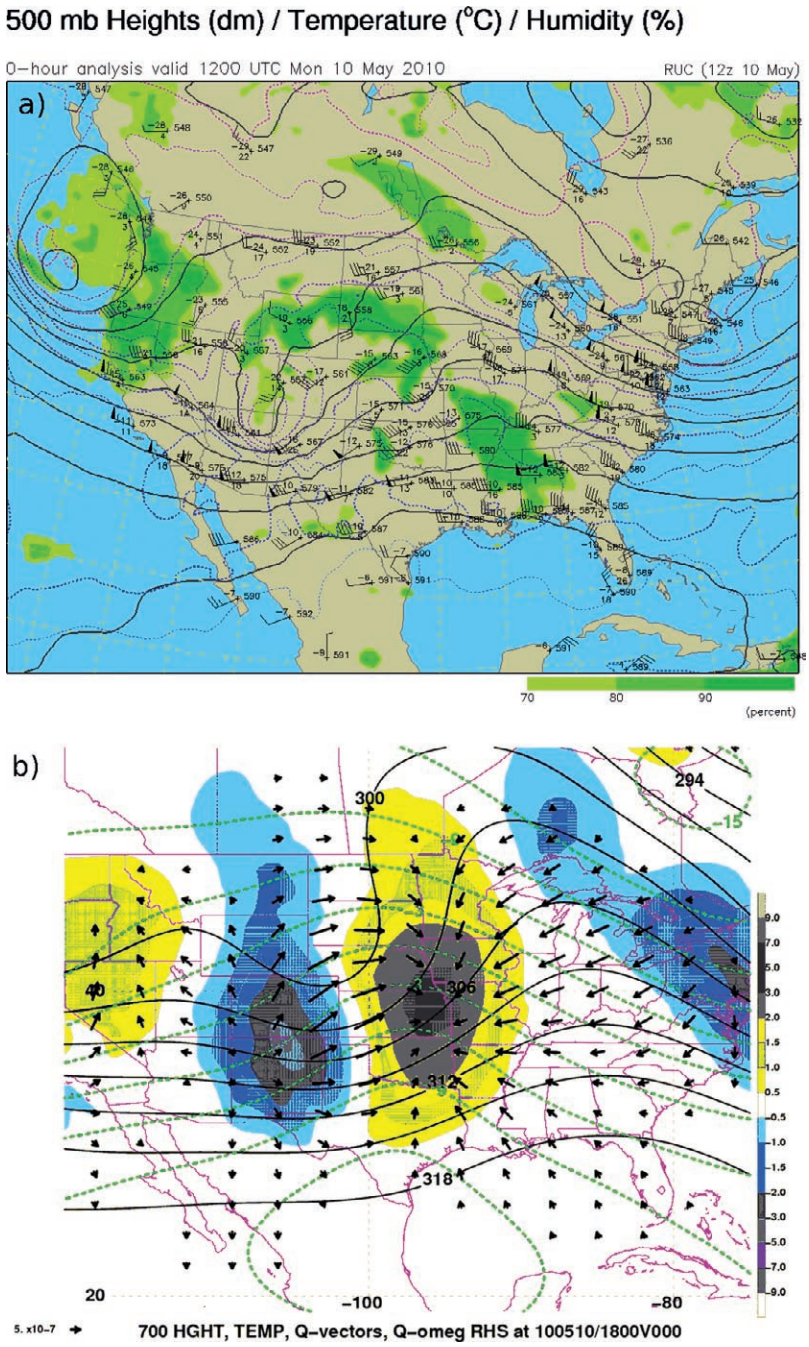

Fig. 3. (a) 500-hPa analysis at 1200 UTC (courtesy of the National Center for Atmospheric Research) and (b) heights at 700 hPa (solid lines in dam), Q-vectors (magnitude in Pa m^{-1} s^{-1}), and quasigeostrophic vertical forcing function resulting from Q-vector convergence (color scale in 10^{-12} Pa m^{-2} s^{-1}) at 1800 UTC 10 May 2010. Flags, wind barbs, and half wind barbs denote 25, 5, and 2.5 m s^{-1}, respectively. Height is plotted in dam, and temperature and dewpoint depression are plotted in °C. The humidity scale is shown at lower right. The 700-hPa analysis is based on smoothed data (1° × 1° data smoothed by a Gaussian weighting function having a weight of 25) from the National Centers for Environmental Prediction (NCEP) Global Forecast System (GFS) (courtesy of T. Galarneau).

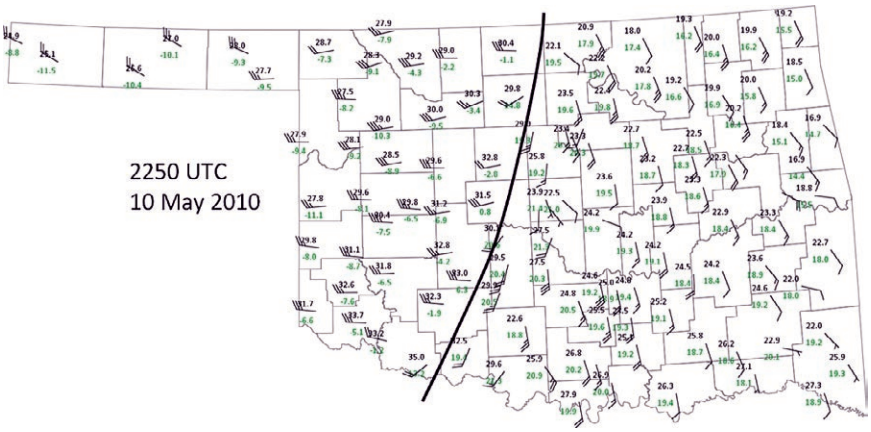

Fig. 4. Surface data from the Oklahoma Mesonet at 2250 UTC 10 May 2010. Temperature (black) and dewpoint (green) values are plotted in °C; wind barbs and half wind barbs denote 5 and 2.5 m s^{-1}, respectively; and the solid line marks approximate location of the dryline (courtesy of the Oklahoma Mesonet).

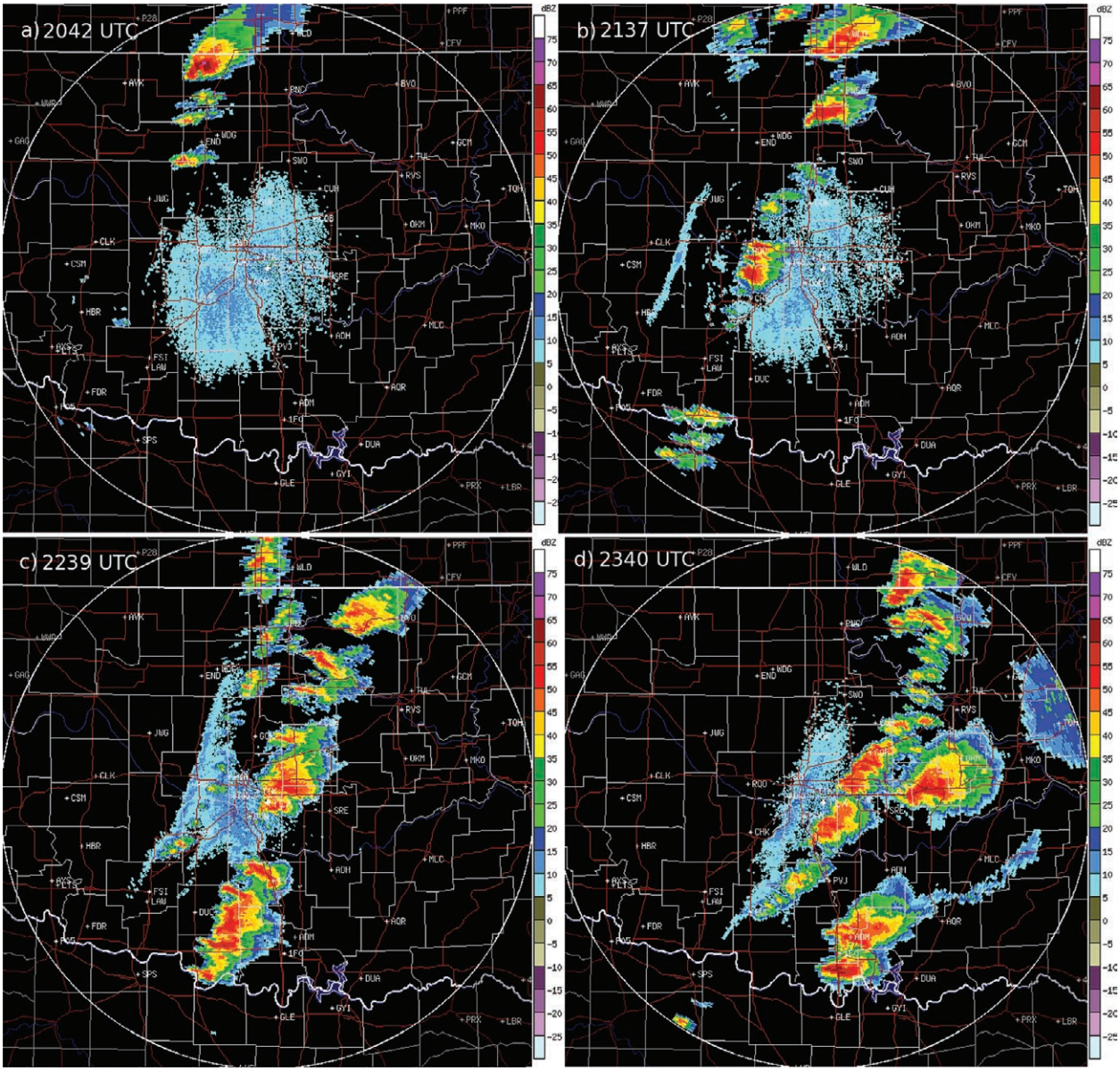

Fig. 5. Radar echoes from the WSR-88D at Twin Lakes, OK (KTLX), at (a) 2042, (b) 2137, (c) 2239, and (d) 2340 UTC 10 May 2010.

Fig. 6. Photograph of OU-PRIME during the construction phase and after completion in Apr 2009. With a 0.45° intrinsic beamwidth, the radar is one of the highest-resolution polarimetric weather radars in the world.

Table 1. Specifications of OU-PRIME compared to polarimetric WSR-88D.

Transmitter		
	OU-PRIME	**WSR-88D polarimetric**
Operating frequency	5510 MHz	2700–3000 MHz
Wavelength	5.44 cm	10.0–11.1 cm
Transmitter power (peak)	1000 kW, 0.1% duty cycle	750 kW, 0.1% duty cycle
Polarization	STSR	STSR
Pulse lengths	0.4–2.0 μs (60–300 m)	1.57, 4.7 μs (235–705 m)
Antenna		
	OU-PRIME	**WSR-88D polarimetric**
Diameter	8.5 m	8.5 m
Intrinsic beamwidth	0.45° at −3 dB	0.9° at −3 dB
Gain	50 dB	44.5 dB
First sidelobe level	Better than −27 dB	Better than −27 dB
Cross-polar isolation	Better than −35 dB	Better than −35 dB
Rotation rate	30° s^{-1} max	36° s^{-1} max
Receiver		
	OU-PRIME	**WSR-88D polarimetric**
Min detectable signal	−112 dBm	−113 dBm
A/D convertor bits	16 bit	16 bit
Gate spacing	25–500 m	250 m
Data format	Moments Real-time complex voltage processing	Moments Real-time complex voltage processing

function of Φ_{DP} (e.g., Hubbert et al. 2010a,b; Zrnić et al. 2010). This contamination can result from errors in the antenna itself or from the presence of a depolarizing medium, such as canted precipitation particles (e.g, Ryzhkov and Zrnić 2007). A competing polarimetric configuration is the alternating transmit–simultaneous receive (ATSR) mode, which allows measurement of the full backscattering covariance matrix. However, the required high-powered switch of the ATSR configuration can present a significant hardware challenge. For this reason, the ATSR mode may be more applicable for dual-transmitter systems or polarimetric phased-array radars with distributed, low-powered transmitters (Zhang et al. 2009).

Pulse lengths for OU-PRIME can be selected over the range 0.4–2 μs, resulting in a range resolution as small as 60 m, which can be oversampled to produce resolution volume spacing as close as 25 m. Combined with the intrinsic angular resolution of 0.45°, OU-PRIME offers extremely high spatial resolution compared to most polarimetric weather radars. The heavy-duty pedestal has complete hemispherical coverage, allowing vertical pointing ("bird bath") for polarimetric calibration. Scan rates can reach 30° s^{-1} with flexibility for range–height indicator (RHI) modes, sector scans, etc.

During the 10 May outbreak, rapid sector scanning was used in an attempt to produce data with high temporal resolution, with volumetric update times of between 2 min 20 s and 2 min 40 s and about 20 s between tilts. For the data presented herein, the radar was operated with a pulse length of 125 m and a maximum unambiguous velocity of 16 m s^{-1}. Data from the nearby S-band research polarimetric WSR-88D operated by NSSL (KOUN) from 10 May 2010 are also presented. Volumetric update times for KOUN data were 4 min 20 s.

Radar performance. Since its commissioning, OU-PRIME has been undergoing extensive testing and has run continuously. Its high-performance and high-quality data are made possible by its unique hardware specifications (Table 1). Because of a combination of a high-gain antenna and stronger scattering at the shorter C-band radar wavelength, OU-PRIME is more sensitive than the nearby S-band KOUN by approximately 10 dB (excluding attenuation effects). Although scan rate and dwell time, in part, control the overall effective beamwidth, OU-PRIME's 0.45° intrinsic beamwidth provides extremely high angular resolution. Other narrow beamwidth polarimetric radars exist, including the polarimetric operational radar in King City, Ontario, Canada, and the Chilbolton S-band radar in the United Kingdom. Because of the narrow beamwidth, longer volumetric update times are required to avoid gaps in scanning. During the 10 May 2010 event, the scanning strategy allowed gaps in elevation angle to maintain a relatively quick update time. Calibration of differential reflectivity is straightforward and manageable because OU-PRIME is capable of pointing its antenna vertically. Such vertical-pointing data show that the two polarization channels are well balanced: only a 0.1-dB correction of Z_{DR} was required for this dataset. OU-PRIME's ability to archive and process the complex voltage signal from the radar (called level 1 or time series data) allows for advanced signal processing studies. These high-performance characteristics are well reflected in the polarimetric radar data collected thus far.

Figure 7 shows an example of OU-PRIME data from a supercell located 15 km from OU-PRIME at 2247 UTC. For comparison, the first row shows 0.87°-tilt KOUN (S band) reflectivity Z_H, differential reflectivity Z_{DR}, and copolar cross correlation coefficient ρ_{hv} at 2246 UTC, and the second row shows the same radar variables measured by OU-PRIME at the 1.0° tilt, one minute later. In Fig. 7, large differences in Z_H, Z_{DR}, and ρ_{hv} between the two radar wavelengths are caused by differences in attenuation, differential attenuation, and non-Rayleigh scattering. Although KOUN reflectivity shows the two tornadoes, OU-PRIME data reveal more detailed polarimetric radar signatures with its finer resolving capability, such as the more detailed structure of the hook echo. The hook echo region is more clearly indicated in the OU-PRIME reflectivity image, and the large particle region is easily identified in the Z_{DR} image. The larger range of measured ρ_{hv} in precipitation at C band compared to S band provides extra information for characterizing and quantifying precipitation microphysics. At S band, typical values of ρ_{hv} are between 0.9 and 1.0 for hydrometeors, with $\rho_{hv} > 0.97$ for rain and lower values for wet hail and melting snow. Because of stronger non-Rayleigh scattering effects at C band, ρ_{hv} values for rain and hail are often below 0.97 and 0.9, respectively. Hence, the range is larger at C band than at S band, which makes C-band measurements of ρ_{hv} more sensitive to larger raindrops and small melting hail than those at S band. This enhanced sensitivity to big drops could be exploited in future research efforts to retrieve the drop size distribution using ρ_{hv}; in pure rain, lower values of ρ_{hv} indicate larger variations of backscattering differential phase within the radar sampling volume, perhaps implying a broader spectrum of sizes with greater relative contributions from the larger drops.

Polarimetric radar variables estimated from auto- and cross-correlation functions of radar signals at zero time lag can be significantly affected by noise, especially when the signal-to-noise ratio (SNR) is low (<10 dB). This substantially limits the usage of observed polarimetric radar data, which has inspired new advanced signal processing studies to improve data quality (Melnikov and Zrnić 2007). Because the estimates at other lags may have useful information, the OU team is developing a multilag estimator (Zhang et al. 2004; Lei et al. 2009) in which correlations at multiple lags are optimally combined to estimate radar moments. To show the effectiveness of the multilag estimator, we compare the ρ_{hv} results for a larger domain in Fig. 8. The figure reveals that ρ_{hv} obtained from the lag-0 estimator has a negative bias in low SNR regions if no correction for noise is made. Although the lag-1 estimates are not biased by noise, they have larger statistical fluctuations compared to the results obtained using the multilag estimator (Fig. 8d). The new estimator reduces statistical fluctuations by adaptively determining the number of useful lags for optimal moment estimation. The greatest improvements are observed in regions with narrow spectra (e.g., stratiform parts of the storm) at farther ranges. The multilag estimator also improves the estimation of other polarimetric radar variables,

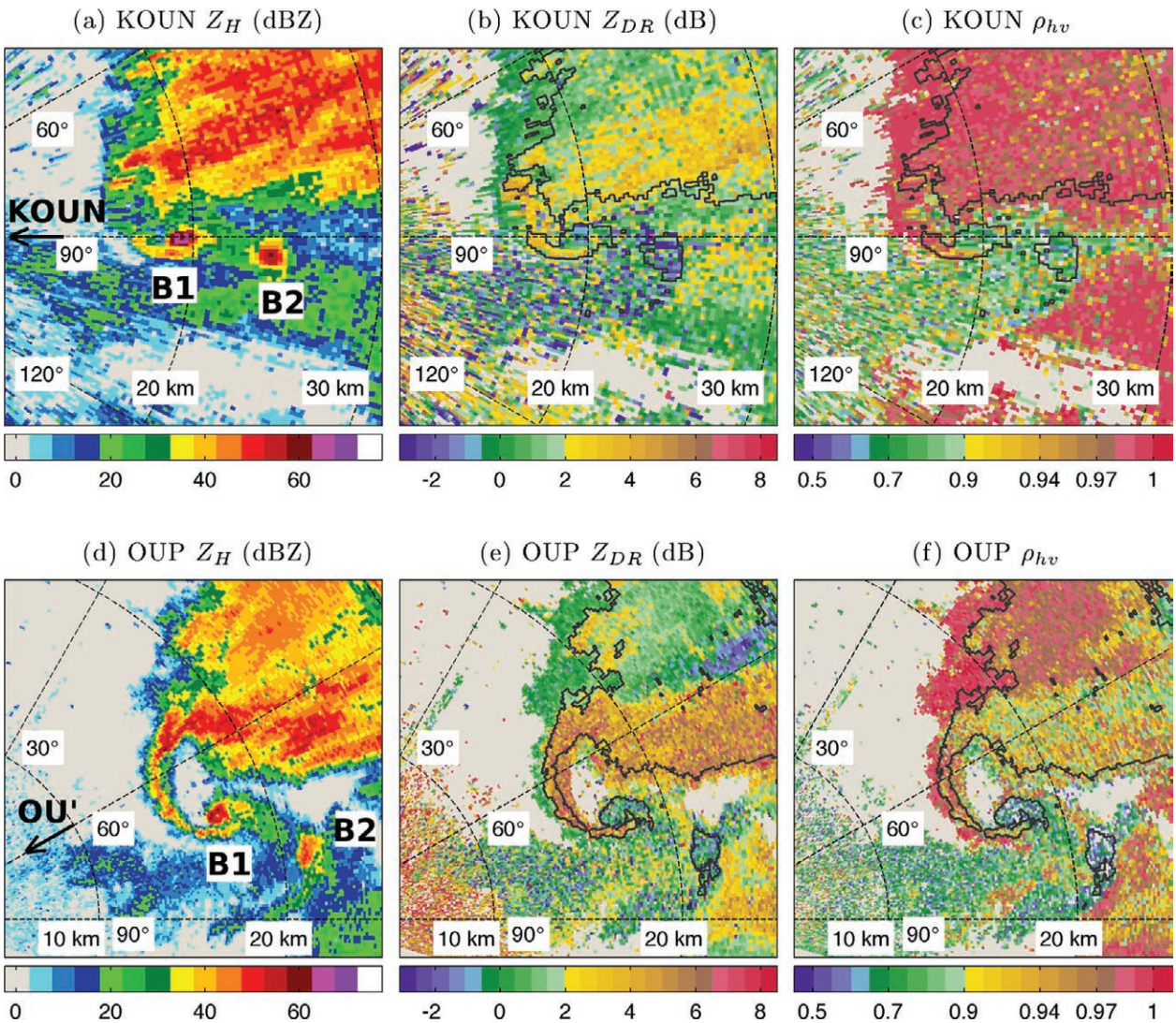

Fig. 7. High-quality polarimetric radar measurements with OU-PRIME (1.0° tilt) at 2247 UTC in comparison with that of KOUN (0.87° tilt) for the tornadic storm at 2246 UTC 10 May 2010. Shown are (top) KOUN and (bottom) OU-PRIME measurements of (a) Z_H, (b) Z_{DR}, and (c) ρ_{hv}. The solid black contour indicates the 30-dBZ contour of reflectivity, and tornadoes B1 and B2 are labeled on reflectivity. Range markers are shown every 10 km, and the locations of KOUN and OU-PRIME (denoted here as OU′) are denoted by the black arrows in (a) and (d), respectively.

such as spectrum width and differential reflectivity (not shown). The OU-PRIME data resulting from the new multilag estimation and the high spatial resolution of the radar have great potential for new studies of storm microphysics and dynamics, as will be shown in the next section.

APPLICATIONS OF OU-PRIME DATA FROM 10 MAY 2010. OU-PRIME collected high-resolution polarimetric radar data on numerous supercells and tornadoes, including several strong and violent tornadoes. The supercell that produced an EF-4 tornado in Norman, Moore, and southern Oklahoma City was observed by OU-PRIME throughout tornadogenesis and the lifetime of this long-track tornado. OU-PRIME collected five tilts in the lowest 1 km during tornadogenesis, providing important data to study the low-level winds through single- and dual-Doppler analyses. This dataset provides an opportunity to investigate polarimetric signatures of supercells and tornadoes and examine how these signatures evolve throughout the life of these storms. The large number of tornadoes and range of tornado intensities provide a great dataset to develop and test robust tornado detection algorithms on several independent tornado cases. These studies may culminate in an improved understanding of tornadogenesis and improved tornado detection.

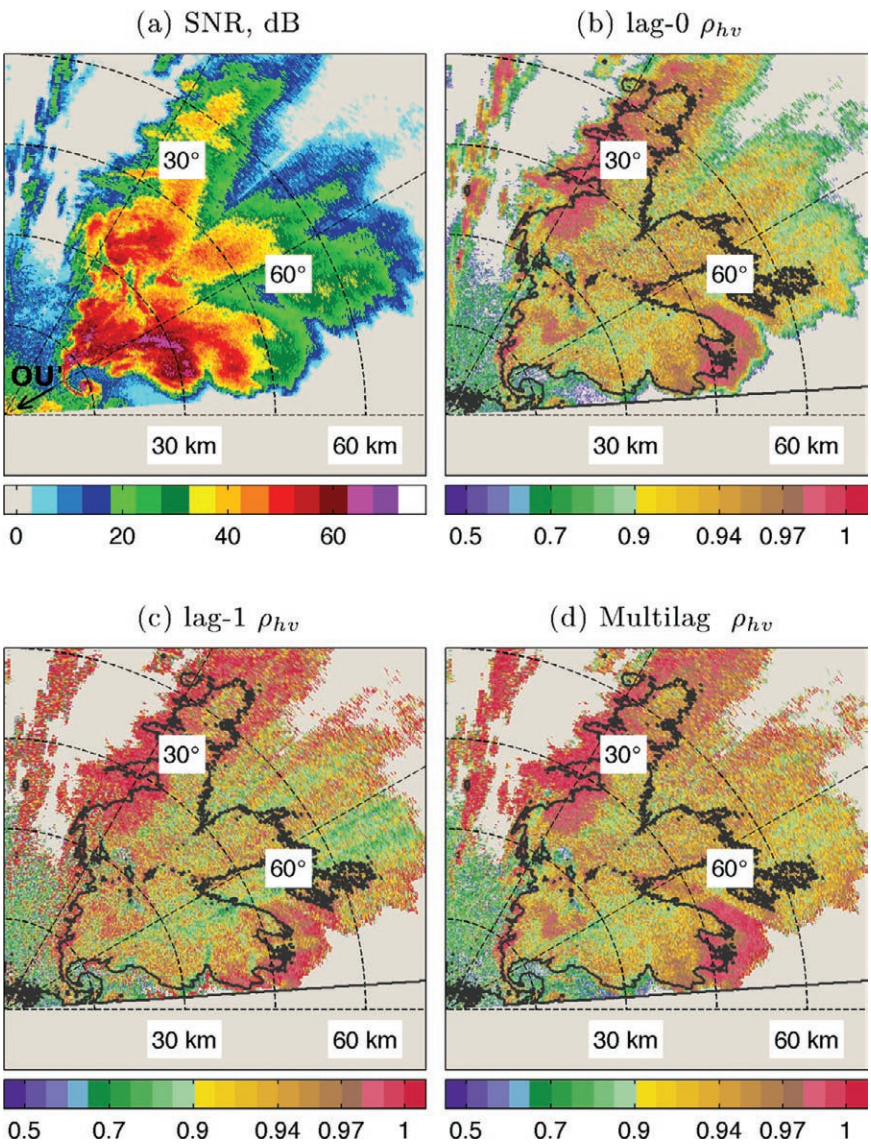

Fig. 8. Comparison of 1.0°-tilt OU-PRIME ρ_{hv} with different estimators at 2242 UTC 10 May 2010. (a) SNR, (b) lag-0 estimator, (c) lag-1 estimator, and (d) multilag estimator. Range rings are plotted every 15 km, the 30-dBZ reflectivity is plotted by a solid black line, and the location of OU-PRIME (denoted as OU′) is denoted by the black arrow in (a).

OU-PRIME observations of tornadogenesis of the Moore, Oklahoma, supercell. A large EF-4 tornado passed through Norman, Moore, and southern Oklahoma City, causing significant damage (tornado A1). In this section, the evolution of this supercell (storm A) during tornadogenesis is presented between 2215 and 2226 UTC, and its interaction with a supercell to its south (storm B) is discussed.

At 2215 UTC, storm A exhibited a contorted reflectivity appendage on its southwest flank (Fig. 9a). Storm A's reflectivity appendage and the rear-flank downdraft (RFD) gust front move southeast (in a storm-relative sense) between 2215 and 2226 UTC as the low-level mesocyclone intensifies. Between 2215 and 2226 UTC, hydrometeors are drawn northward from the forward-flank downdraft (FFD) precipitation echo of storm B, eventually wrapping into the low-level mesocyclone (Fig. 9a). At 2226 UTC, a secondary gust front forms behind the

primary RFD gust front (Fig. 9b), forming a double rear-flank gust front structure. The role of the RFD and FFD in tornadogenesis can be investigated, aided by polarimetric observations to study the thermodynamic characteristics of these downdrafts (Romine et al. 2008) by inferring the degree of melting of hail (Ryzhkov et al. 2009) or evaporation of rain (Kumjian and Ryzhkov 2010).

The excellent angular resolution and high sensitivity of OU-PRIME revealed numerous small-scale azimuthal shear zones along storm A's trailing RFD gust front, which may indicate the presence of vortices. Small-scale vortices along the RFD gust front have been documented by mobile radars (Bluestein et al. 1997, 2003; Marquis et al. 2008), and the role of these vortices in providing a "seed" for tornadogenesis was hypothesized by Bluestein et al. (2003). Storm A develops azimuthal shear zones along the RFD gust front as the RFD penetrates into the inflow region and convergence increases significantly. These azimuthal shear zones are observed at 2220 UTC, where the 1.0° tilt reveals numerous small-scale (about 200–300 m in diameter) and larger-scale azimuthal shear zones (on the order of 1 km in diameter) along the RFD gust front at about 200 m AGL (Fig. 10a). At the 4.0°-tilt radial velocity field at 2221 UTC (Fig. 10b; 800–900 m AGL), only the larger diameter azimuthal shear zones are observed. The dense, low-level sampling may facil-

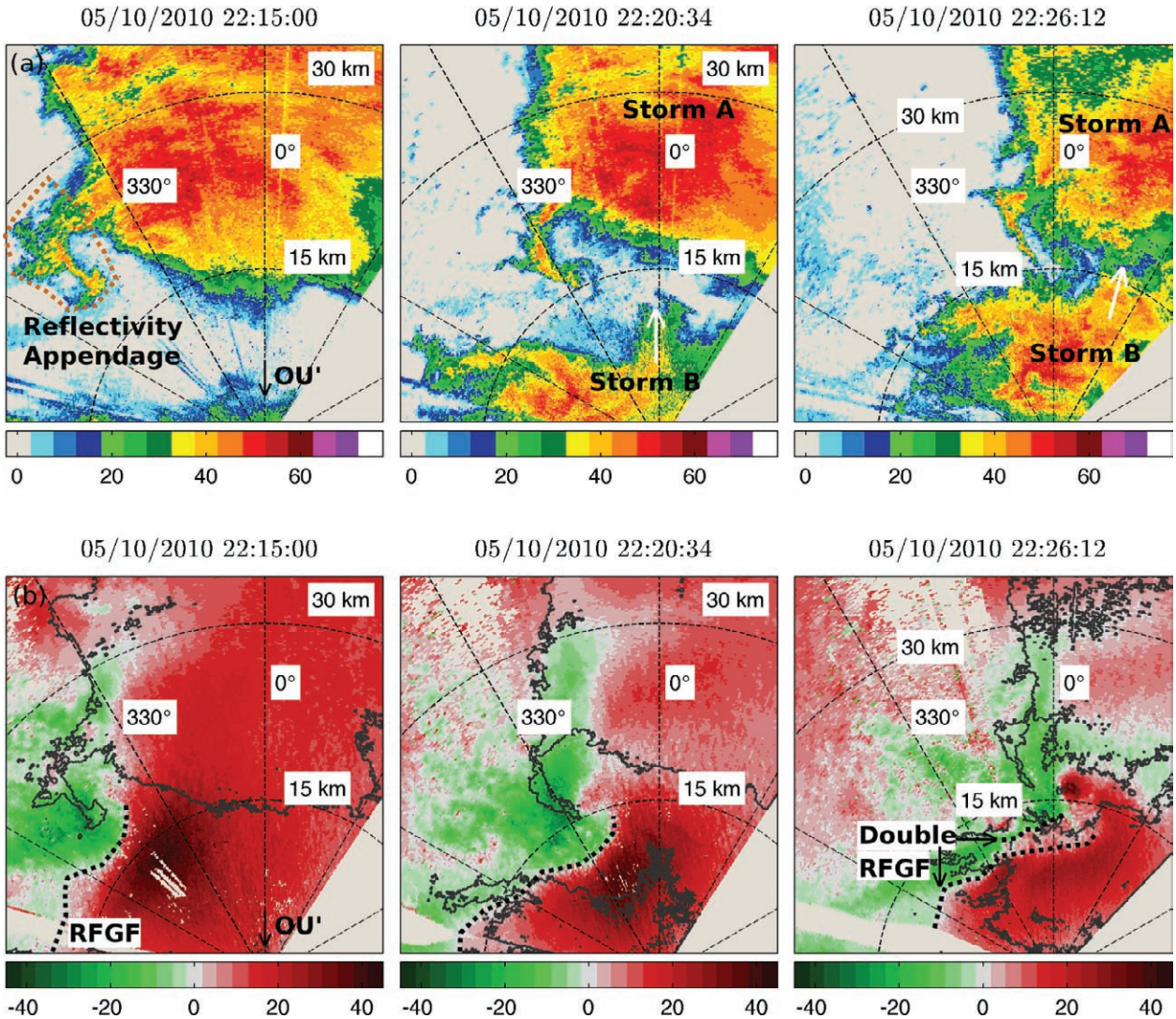

Fig. 9. The 0.2°-tilt (a) reflectivity Z_H and (b) radial velocity v_r from OU-PRIME at 2215, 2220, and 2226 UTC 10 May 2010. Range rings are plotted every 15 km, and the black arrow points to the radar location. The brown stippled line highlights the location of the reflectivity appendage at 2215 UTC, and the white arrows show the region of precipitation wrapping into the low-level mesocyclone at 2220 and 2226 UTC. The RFD gust front position is denoted by the black stippled line, and a double gust-front structure is observed at 2226 UTC.

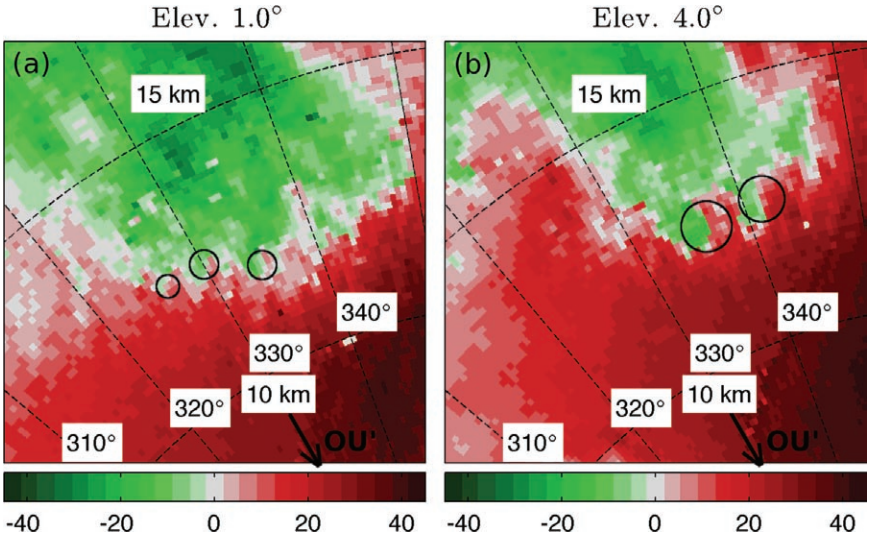

Fig. 10. The (a) 1.0°- and (b) 4.0°-tilt radial velocity v_r from OU-PRIME at 2220 and 2221 UTC 10 May 2010. Some stronger regions of cyclonic shear are shown within the black circles. The range rings are every 5 km, and the arrow points toward the location of OU-PRIME.

itate studies of the change in vortex scale with height and perhaps their role in tornadogenesis, if any.

OU-PRIME observations of prolific tornado-producing supercells. Storm B (the southern supercell) had two tornadoes ongoing during the 2244 UTC volume scan: an EF-4 tornado that heavily damaged portions of southern and eastern Norman and began within 200 m of the NWC and OU-PRIME and another EF-2 tornado just to its east-southeast. The high-resolution OU-PRIME reflectivity data (Fig. 11a) reveal a thin, elongated hook echo wrapping into the western tornado (tornado B1). Moderate Z_H and high Z_{DR} (Fig. 11c) values in the hook echo indicate a convective-like drop size distribution characterized by a large median drop size. The observed ρ_{hv} values > 0.95 (and even higher at S band) suggest the thin echo appendage may be mainly rain filled, though the presence of small melting hail cannot be ruled out (Fig. 11d). On the western periphery of the hook echo, a band of lower Z_H, lower Z_{DR}, and higher ρ_{hv} indicates a distribution of predominantly smaller drops.

The eastern tornado (tornado B2) developed along the RFD gust front in the absence of significant reflectivity aloft, ostensibly removed from the storm B's main updraft. The authors speculate that tornado B2 may have formed beneath a newly developed convective updraft along the RFD gust front. By 2244 UTC, however, tornado B2 was beneath the bounded weak echo region of storm B (not shown). Both tornadoes exhibit a clear tornadic debris signature (TDS; Ryzhkov et al. 2002, 2005c; Bluestein et al. 2007; Kumjian and Ryzhkov 2008) with high Z_H, low Z_{DR}, and low ρ_{hv}, collocated with intense cyclonic shear in radial velocity (Fig. 11b). The TDS extends through the highest tilt, revealing that debris is lofted to at least 2.4 km AGL. Intriguingly, tornado B2 is collocated with a much larger TDS, even though tornado B1 produced more significant damage. An explanation for this difference is that tornado B1 was enshrouded with precipitation, likely obscuring the TDS and aiding in debris fallout, whereas tornado B2 remained in a region of little or no precipitation and beneath strong inflow and updraft. Moreover, the RFD gust front is demarcated by the sharp transition between low and high ρ_{hv}, likely attributed to light debris lofted by very strong RFD winds (about 40 m s^{-1} at the lowest tilt) behind the gust front and light rain ahead of it.

In addition to the tornadoes, storm B exhibited several prominent supercell polarimetric signatures at 2244 UTC. At the lowest tilt, a Z_{DR} arc extended along the reflectivity gradient on the southern edge of the FFD (Fig. 11c). Very high Z_{DR} values (>8 dB) are observed on the eastern edge of the FFD, even in regions with lower Z_H (<25 dBZ). Such features are distinctive of supercell storms and indicate a drop size distribution dominated by large drops with a deficit of smaller drops, caused by size sorting due to strong vertical wind shear according to Kumjian and Ryzhkov (2008, 2009). The negative Z_{DR} values just north of the Z_{DR} arc are due to differential attenuation, which was significant at times (<–8 dB).

The Z_{DR} arc (Fig. 12) undergoes an evolution similar to that of a cyclic supercell presented in Kumjian et al. (2010). Between 2244 and 2247 UTC, the Z_{DR} arc is disrupted closer to the updraft by a narrow strip of low (<1 dB) Z_{DR} (Fig. 12b) and high ρ_{hv} (not shown), implying an influx of smaller drops, whereas further along the FFD values of Z_{DR} increase dramatically to more than 8 dB (though contract in areal extent). After 2247 UTC, the RFD gust front (observed in the Doppler velocities; not shown) surges east and north, pinching off the inflow and occluding both tornadoes (B1 and B2) by 2252 UTC. Moreover, during the same period, radial velocities in the inflow region closest to the tornado increase from

–10 to 10 m s^{-1}, implying a decrease in storm-relative inflow given an approximate storm motion of 260° at 25 m s^{-1} (not shown). Also between 2247 and 2252 UTC, precipitation fills the inflow region (cf. inbound velocities in Fig. 11b), whereas Z_H also increases in the RFD and hook echo, which may imply a weakening updraft (e.g., Lemon and Doswell 1979).

Although the Z_{DR} arc was disrupted during the occlusion, the supercell quickly produces a new Z_{DR} arc. Between 2249 and 2254 UTC, the Z_{DR} arc decreases in size and loses its characteristic arc shape as a "blob" of Z_H with high Z_{DR} forming in the inflow region (Figs. 12c–e), possibly from precipitation now able to fall from the echo overhang because a weakened updraft during the occlusion or from the beginning of a merger with a storm to supercell B's south. This becomes part of the new Z_{DR} arc, which then becomes reorganized into its classic shape by 2259 UTC, wrapping around into the inflow region once again. Such reorganization of the Z_{DR} arc is revealing, because a tornado develops during the reorganization of the Z_{DR} arc, despite the disorganized appearance of Z_H in the RFD (Fig. 12f). Instead of observing a thin hook echo observed with classic supercells (e.g., supercell B at

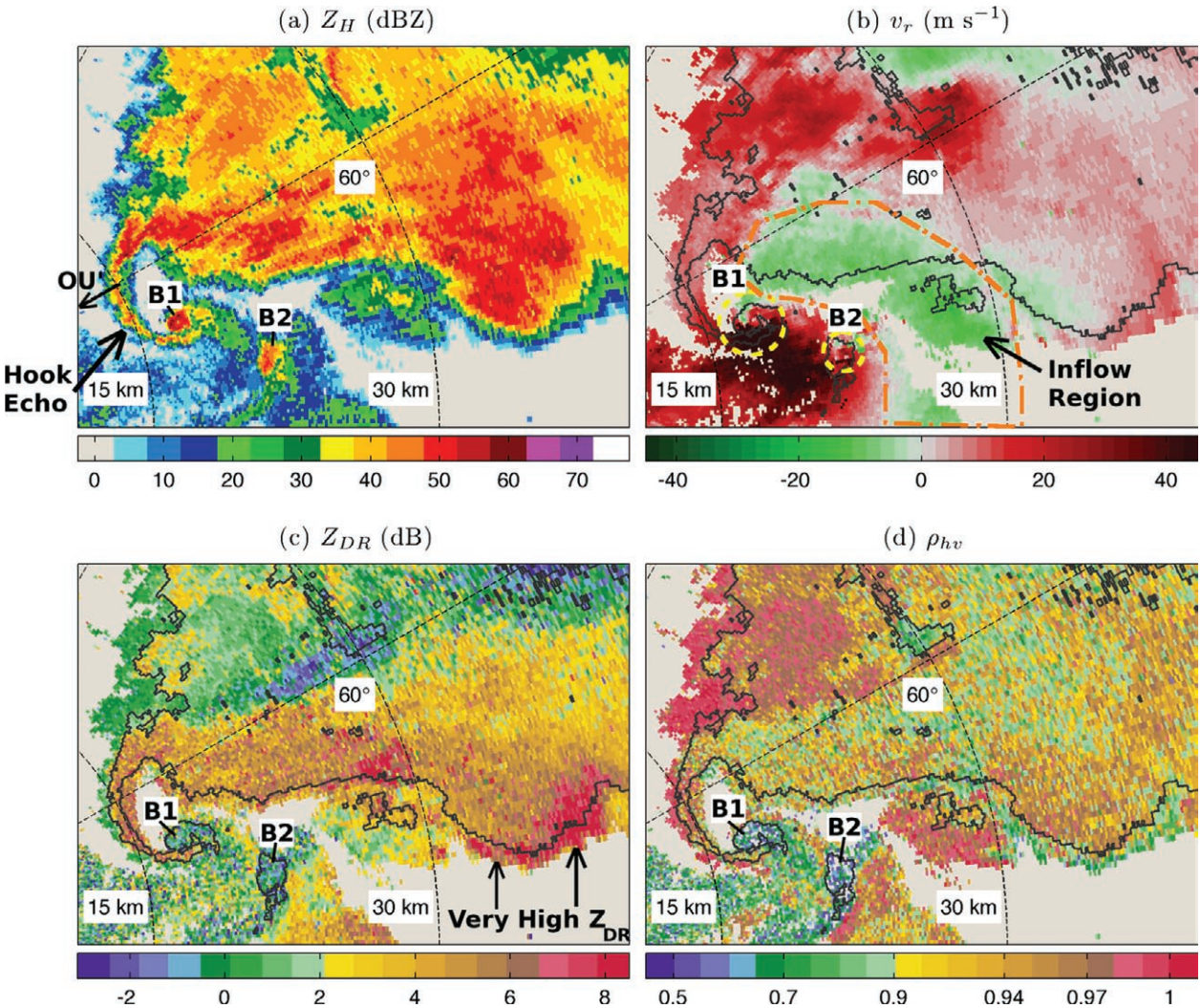

Fig. 11. OU-PRIME measurements of (a) Z_H, (b) v_r, (c) Z_{DR}, and (d) ρ_{hv}, at 1.0° tilt from the sector scan started at 2245 UTC. Range rings, the radar location, and the 30-dBZ reflectivity contour are plotted as described in Fig. 8. A thin hook echo is observed, divided into two distinct drop size distributions. Storm B is producing two tornadoes, and the locations of tornadoes B1 and B2 are labeled and yellow circles show the locations of the shear signatures in (b). Both tornadoes produced tornadic debris signatures, evident by high Z, near-zero Z_{DR}, and low ρ_{hv}. A prominent Z_{DR} arc is observed extending along the southern part of storm B's FFD, and very high Z_{DR} values (Z_{DR} > 8 dB) are seen on the eastern edge of the FFD. The inflow region is roughly demarcated by the orange dashed line.

2244 UTC), the precipitation in the RFD is occurring over a broad region (i.e., large area covered by the 30-dBZ Z_H contour in Fig. 12f).

Farther aloft at 2259 UTC, the Z_{DR} and ρ_{hv} half rings are evident at 6.4°, emanating from an elongated bounded weak echo region (Fig. 13), as well as anomalously large attenuation (<–25 dB) and differential attenuation at the northern terminus of the ring. Kumjian and Ryzhkov (2008) define these midlevel signatures as circular or semicircular "rings" of enhanced Z_{DR} values and decreased ρ_{hv} values, located near or within the updraft and mesocyclone. By the 8.9° tilt (Fig. 14), the Z_{DR} ring has disappeared, indicating that the liquid hydrometeors have frozen, though the ρ_{hv} ring is still apparent. Collocated with the ρ_{hv} depression at this higher tilt are slightly negative Z_{DR} values and high Z_H (>60 dBZ), possibly indicating large hail. Alternating radial streaks of positive and negative Z_{DR} (and higher and lower Φ_{DP} values) farther downstream (Fig. 14) are a result of signal depolarization associated with ice crystals oriented in the storm's strong electrostatic field (Ryzhkov and Zrnić 2007).

Advanced tornado detection. Wang et al. (2008) developed a neuro-fuzzy tornado detection algorithm (NFTDA) for S-band weather radars to improve detection by subjectively considering the tornado's shear and spectral signatures (TSS). The wide and flat tornado spectra observed by pulsed Doppler weather radar were reported by Zrnić and Doviak (1975) and were recently characterized using four parameters (Yu et al. 2007; Yeary et al. 2007). Spectrum width and three other parameters are calculated from the radar's complex voltage signal (level 1 data) based on signal statistics and higher-order spectra, which are not readily available from operational radars or most research radars. Motivated by this fact and the unique polarimetric characteristics of tornadic debris (Ryzhkov et al. 2005c), the NFTDA was modified to use tornado signatures that are directly available or derived from Doppler and polarimetric moments, including velocity difference (to represent

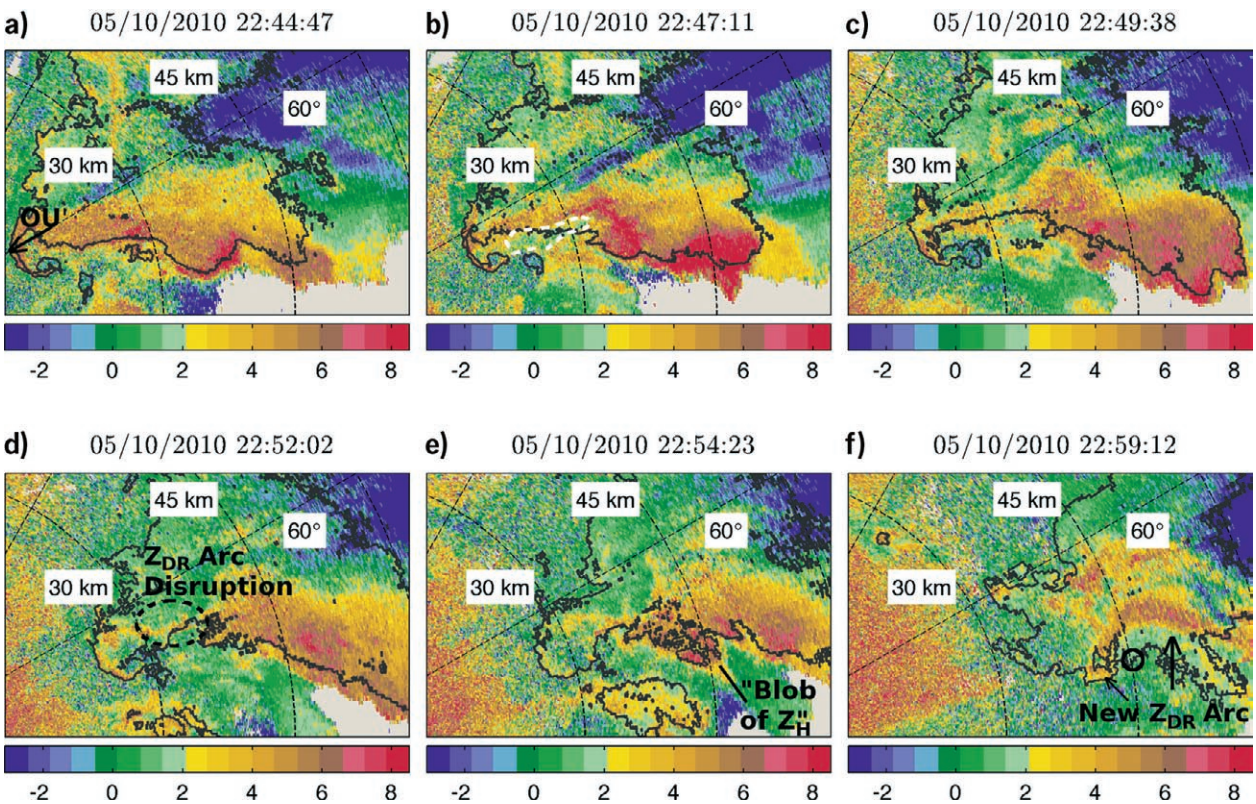

Fig. 12. The evolution of the Z_{DR} during cyclic tornadogenesis, showing the 1.0° tilt at (a) 2244, (b) 2247, (c) 2249, (d) 2252, (e) 2254, and (f) 2259 UTC 10 May 2010. Range rings, the radar location, and the 30-dBZ Z_H contour are plotted as described in Fig. 8. (b) At 2247 UTC, a region of low Z_{DR} is observed along the southern FFD close to the inflow region (white dashed line). (d) By 2252 UTC, the Z_{DR} arc is disrupted, characterized by a contraction in the size of high Z_{DR} values along the FFD. (e) At 2254 UTC, a blob of Z_H with high Z_{DR} is observed along the FFD, which becomes the new Z_{DR} arc. (f) The Z_{DR} arc quickly evolves into a well-defined arc shape by 2259 UTC, wrapping back into the inflow region of the supercell that is producing a new tornado (denoted by the black circle).

the shear signature), spectrum width (to represent the TSS), Z_{DR}, and ρ_{HV} (Wang and Yu 2009). Recently, the NFTDA has been further modified for OU-PRIME with an upgraded rule operator of Sugeno fuzzy inference (Sugeno 1985), which can provide reliable detection even if some of the signatures are weak. In addition, a hybrid neural network (forward pass and backward pass) was implemented to train the membership functions and the weights in a fuzzy logic algorithm (Jang 1993). The least squares method (forward pass) optimizes the membership functions, and the gradient descent method (backward pass) adjusts the weights corresponding to the fuzzy set in the input domain (Jang 1993).

The NFTDA was trained using four volume scans of data collected by OU-PRIME from two tornado cases: 14 May and 13 June 2009. The 14 May data provided a tornado case far from the radar (near Anadarko, Oklahoma, and about 75-km range), and the 13 June data provided a tornado case very close to the radar (about 5 km from OU-PRIME). After carefully examining the reflectivity, the radial velocity, and the damage report, the data are classified into two categories: tornado and nontornado. The training component is an iterative process that is terminated when the NFTDA outputs match the input states and the maximum number of iterations is reached (Wang et al. 2008). In

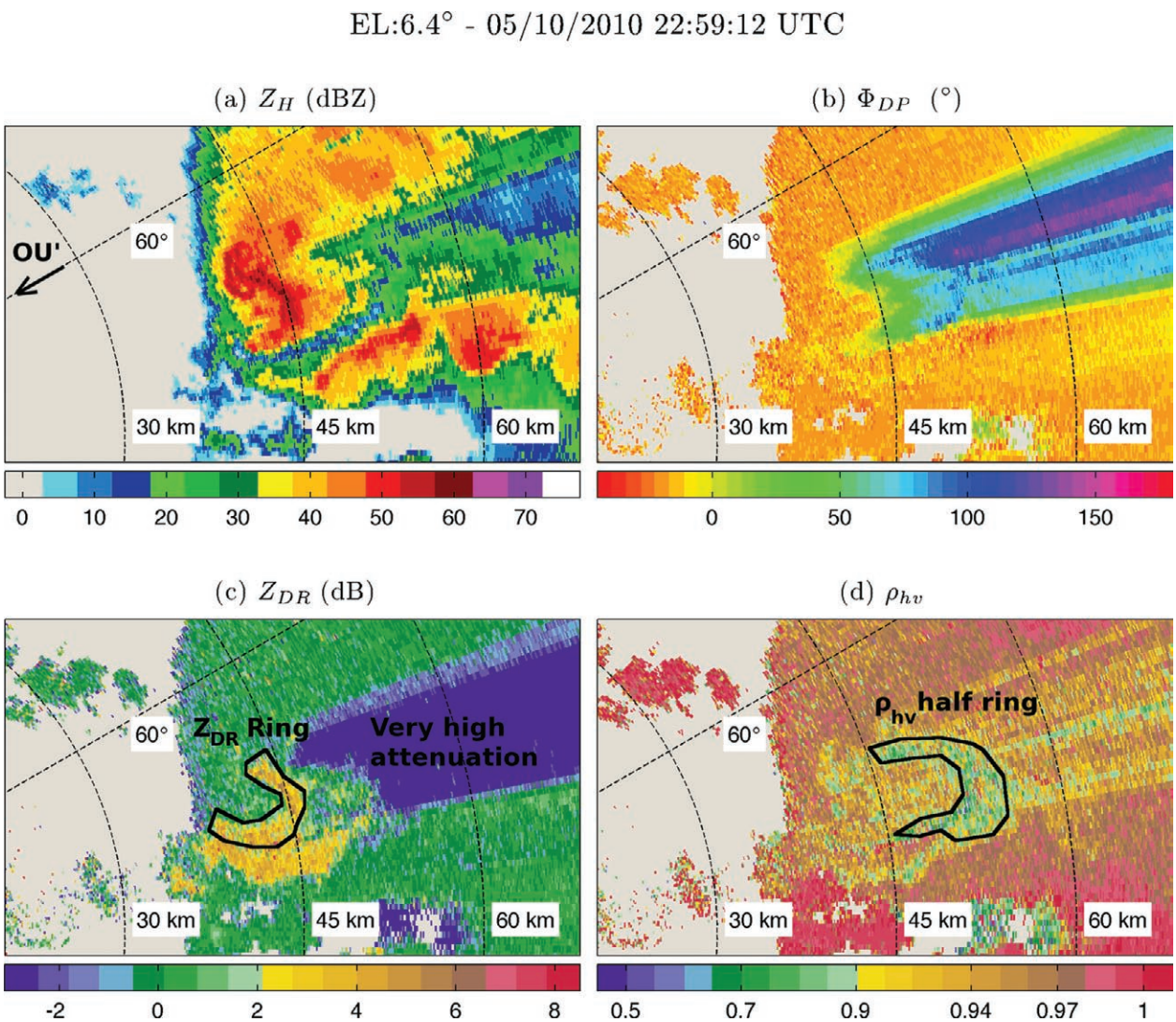

Fig. 13. OU-PRIME measurements of (a) Z_H, (b) Φ_{DP}, (c) Z_{DR}, and (d) ρ_{hv} at the 6.4° tilt at 2259 UTC 10 May 2010. Range rings and the radar location are plotted as described in Fig. 8. The locations of the Z_{DR} and ρ_{hv} half rings are shown by the solid black lines. The Z_{DR} ring is associated with cyclonic advection of hydrometeors around the occluded mesocyclone of storm B, and the ρ_{hv} ring is associated with cyclonic advection of hydrometeors around storm B's new mesocyclone. Very large differential attenuation likely obscures a Z_{DR} ring, which should be collocated with the ρ_{hv} ring.

this work, the NFTDA was tested and verified using data from the 10 May 2010 tornado case. The detection results superimposed on the damage paths are presented in Fig. 15a. OU-PRIME data did not show a tornado debris signature until 2226 UTC (not shown). The first NFTDA detection occurred at 2230 UTC, so missed detections occurred at 2226 and 2228 UTC. These missed detections were associated with low reflectivity and therefore were filtered out by the reflectivity threshold (30 dBZ) in the algorithm. Although lowering the threshold can produce correct detections, the possibility of false detections increases. An EF-3 tornado near Dale, Oklahoma, was not detected between 2248 and 2259 UTC. This tornado's polarimetric signature is much shallower compared to the other tornadoes shown (only lowest tilt shown) and was rejected by the NFTDA's quality control procedure of height continuity. However, during the time period of NFTDA analysis, most of the tornadoes during their strong phases (EF-2 and greater) were detected. The closest and the farthest detections are 13 (2242 UTC) and 32 km (2256 UTC), respectively. Note that storm B was not in the 90° sector scanned by the OU-PRIME until 2242 UTC. All the detections are consistent with the damage path and the analysis in the preceding subsections.

Examples of v_r and σ_v at 2244 UTC are presented in Figs. 15b,c. Several regions of velocity aliasing are evident because of relatively small Nyquist velocity (V_N = 16.06 m s^{-1}). Relatively large spectrum width can also be observed within these regions. In other words, false detections could result if only the velocity difference and spectrum width were used for detection. Although missed detections can result if the tornado does not produce a debris signature, including the debris signature decreases the false-alarm rate (FAR). Similarly, false detections are possible if detections are made from polarimetric signatures alone, where a number of regions with low Z_{DR} and ρ_{HV} can be

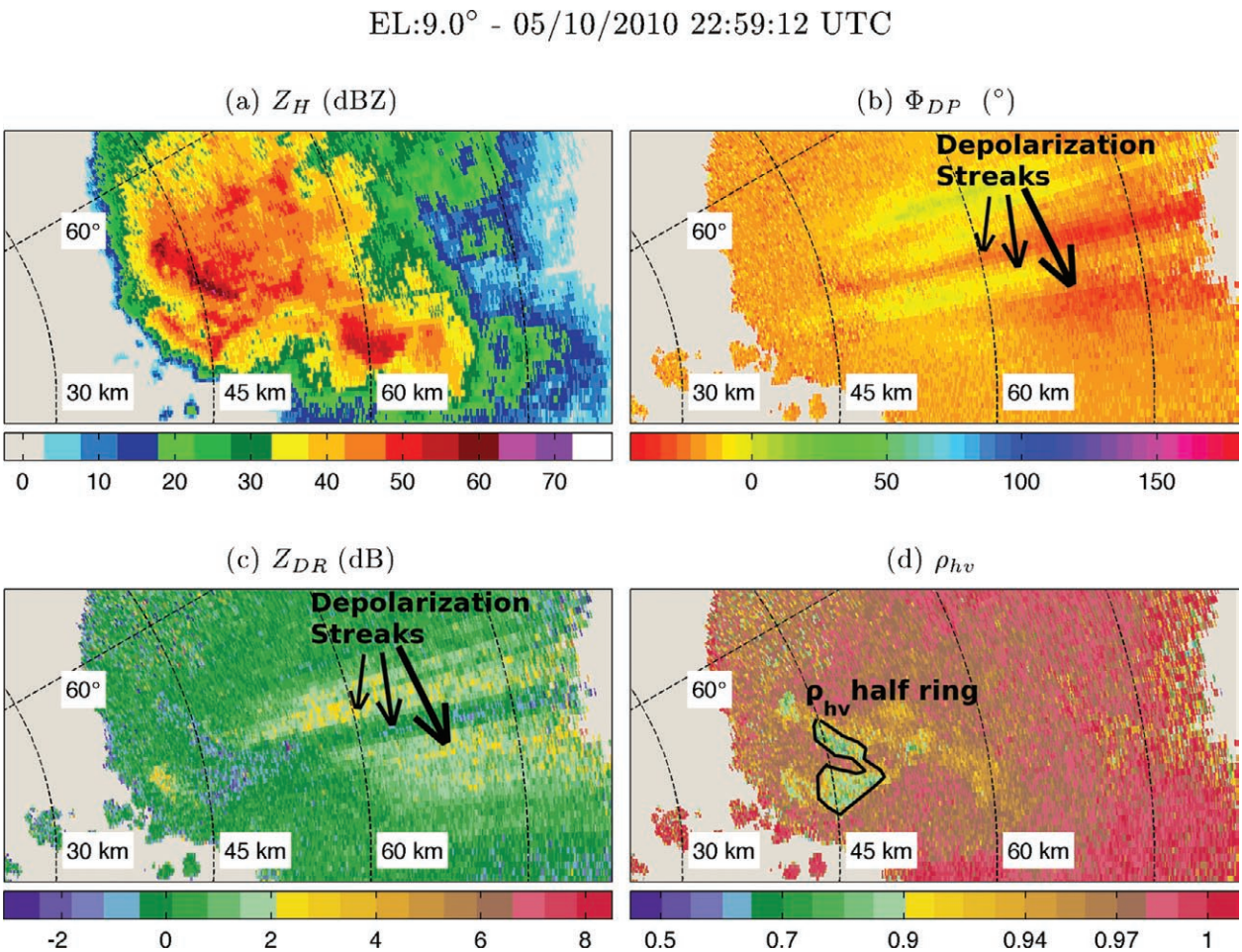

Fig. 14. OU-PRIME measurements of (a) Z_H, (b) Φ_{DP}, (c) Z_{DR}, and (d) ρ_{hv} at the 9.0° tilt at 2259 UTC 10 May 2010. Range rings and the radar location are plotted as described in Fig. 8. Prominent depolarization streaks (alternating positive and negative Z_{DR} values) are evident in differential reflectivity in (c), and streaks are observed in Φ_{DP} in the same location. The solid black line in (d) shows the location of the ρ_{hv} half ring.

observed (cf. Fig. 12). However, the NFTDA combines all available information in a fuzzy logic system to produce three accurate detections at 2244 UTC.

SUMMARY. The 10 May 2010 tornado outbreak devastated parts of Oklahoma with 55 tornadoes, including several strong and violent tornadoes.

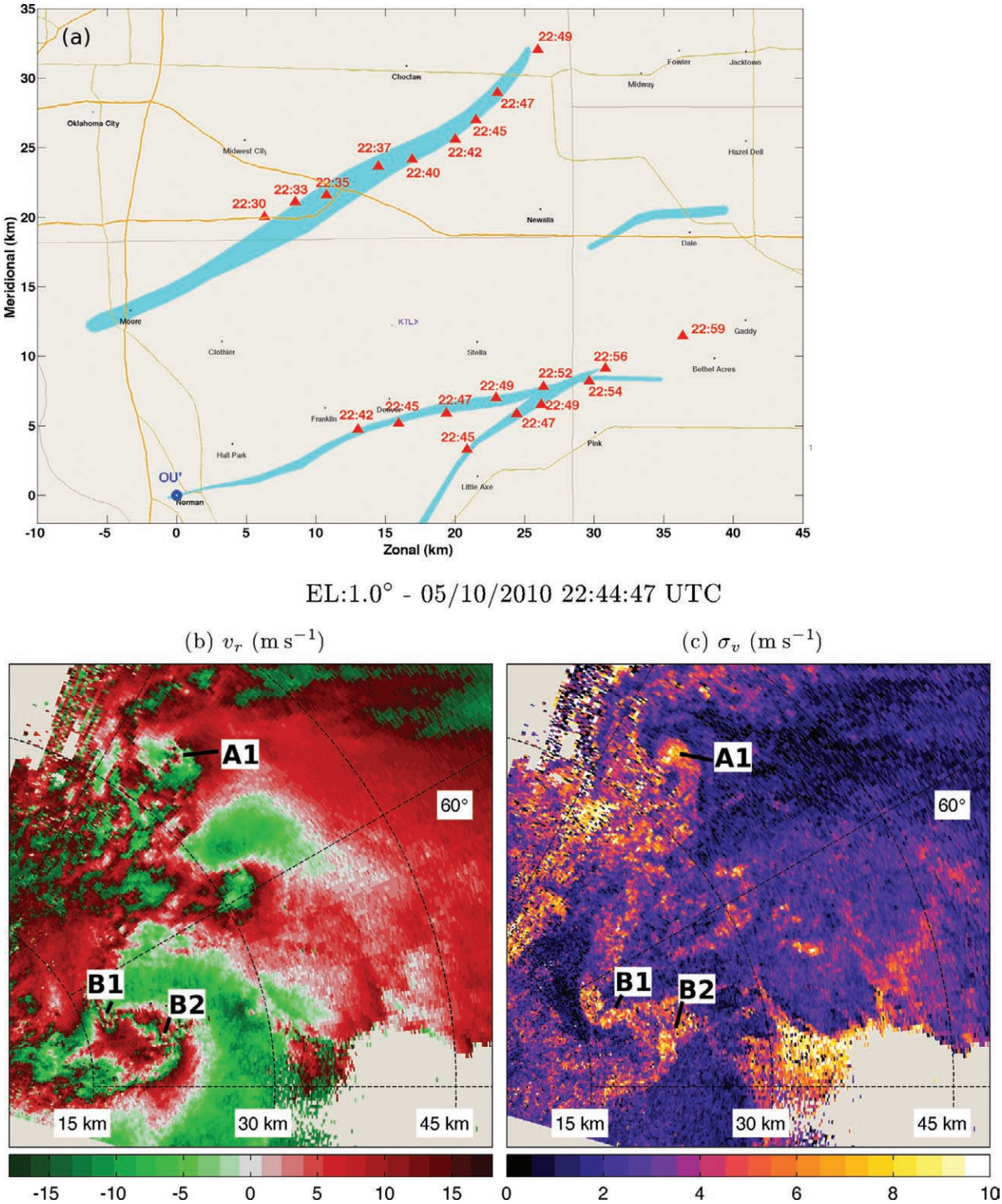

Fig. 15. (a) NFTDA detection results on the tornado outbreaks on 10 May 2010, with tornado detections shown by the red triangles (times shown in UTC). Examples of (b) 1.0°-tilt radial velocity v_r and (c) spectrum width σ_v at 2244 UTC are presented.

Researchers in the ARRC operated OU-PRIME on 10 May 2010, capturing a rare dataset of two cyclic supercells producing four tornadoes of EF-2 to EF-4 intensity near the radar (less than 5 km in one case). The 0.45° intrinsic beamwidth of OU-PRIME, high sensitivity, and the application of the multilag estimation resulted in very high-resolution and high-quality polarimetric data of these supercells and tornadoes.

The 10 May 2010 OU-PRIME dataset has tremendous potential for polarimetric studies of supercells and tornadoes. OU-PRIME collected data at numerous low-level elevation angles during the tornadogenesis of the Moore EF-4 tornado, revealing a contorted reflectivity appendage and relatively small-scale vortices along the RFD gust front prior to tornadogenesis. During tornadogenesis of tornadoes A1 and A2, rain curtains are drawn in from the forward-flank precipitation of storm B, providing an opportunity to investigate the interactions of the two storms. Many supercell polarimetric signatures were also observed in this dataset. The evolution of the Z_{DR} arc was consistent with previous polarimetric observations of cyclic supercells and exhibited a classic shape just prior to tornadogenesis of an EF-3 tornado that struck Tecumseh and Seminole, Oklahoma (Fig. 1). The tornadoes exhibited obvious TDSs (low ρ_{hv} and low Z_{DR}), and the TDSs varied in horizontal and vertical extent. The NFTDA tornado detections agreed well with the National Weather Service (NWS) damage paths for most of the tornadoes with EF-2 intensity or greater.

Researchers at the ARRC, OU, and collaborating institutions have started analyzing this unique dataset. Future efforts with this dataset include investigating the evolution of substorm-scale vortices, low-level winds during tornadogenesis, and polarimetric signatures associated with the supercells and tornadoes. New schemes may be developed for detecting hail, determining hail size, and correcting attenuation at C band. Furthermore, efforts to assimilate the polarimetric radar measurements are underway to assess the possible benefits of polarimetric data in numerical models (Jung et al. 2008a,b). These studies have the potential to advance our understanding of tornadogenesis, storm structure, and interactions and to discover new applications of polarimetric radar in meteorology and engineering.

ACKNOWLEDGMENTS. The authors thank the administration of the University of Oklahoma (OU), which supported the development of OU-PRIME and other facilities at OU. OU-PRIME is maintained and operated by OU's Atmospheric Radar Research Center (ARRC) and was built to OU specifications by Enterprise Electronics Corporation (EEC). Robert Palmer was partially supported by the National Science Foundation through Grant AGS-0750790. H. Bluestein was supported in part by NSF Grant AGS-0934307. Tom Galarneau (University of Albany) provided quasigeostrophic diagnostic calculations of the synoptic-scale forcing seen in Fig. 3. The authors also thank Doug Speheger for providing the shape files of the damage paths. Don Burgess and two anonymous reviewers provided constructive comments and suggestions that improved the clarity and layout of the paper.

REFERENCES

Biggerstaff, M. I., and Coauthors, 2005: The Shared Mobile Atmospheric Research and Teaching radar: A collaboration to enhance research and teaching. *Bull. Amer. Meteor. Soc.,* **86,** 1263–1274.

Bluestein, H. B., and W. P. Unruh, 1989: Observations of the wind field in tornadoes, funnel clouds, and wall clouds with a portable Doppler radar. *Bull. Amer. Meteor. Soc.,* **70,** 1514–1525.

——, A. L. Pazmany, J. C. Galloway, and R. E. McIntosh, 1995: Studies of the substructure of severe convective storms using a mobile 3-mm-wavelength Doppler radar. *Bull. Amer. Meteor. Soc.,* **76,** 2155–2169.

——, S. G. Gaddy, D. C. Dowell, A. L. Pazmany, J. C. Galloway, R. E. McIntosh, and H. Stein, 1997: Doppler radar observations of substorm-scale vortices in a supercell. *Mon. Wea. Rev.,* **125,** 1046–1059.

——, C. C. Weiss, and A. L. Pazmany, 2003: Mobile Doppler radar observations of a tornado in a supercell near Bassett, Nebraska, on 5 June 1999. Part I: Tornadogenesis. *Mon. Wea. Rev.,* **131,** 2954–2967.

——, M. M. French, R. L. Tanamachi, S. Frasier, K. Hardwick, F. Junyent, and A. Pazmany, 2007: Close-range observations of tornadoes in supercells made with a dual-polarization, X-band, mobile Doppler radar. *Mon. Wea. Rev.,* **135,** 1522–1543.

——, ——, I. Popstefanija, R. T. Bluth, and J. B. Knorr, 2010: A mobile, phased-array Doppler radar for the study of severe convective storms: THE MWR-05XP. *Bull. Amer. Meteor. Soc.,* **91,** 579–600.

Bodine, D., P. L. Heinselman, B. L. Cheong, R. D. Palmer, and D. Michaud, 2010: A case study on the impact of moisture variability on convection initiation using radar refractivity retrievals. *J. Appl. Meteor. Climatol.,* **49,** 1766–1778.

Borowska, L., A. Ryzhkov, D. Zrnić, C. Simmer, and R. Palmer, 2011: Attenuation and differential attenuation of the 5-cm-wavelength radiation in melting hail. *J. Appl. Meteor. Climatol.,* **50,** 59–76.

Brandes, E. A., 1984: Vertical vorticity generation and mesocyclone sustenance in tornadic thunderstorms:

The observational evidence. *Mon. Wea. Rev.,* **112,** 2253–2269.

——, G. Zhang, and J. Vivekanandan, 2002: Experiments in rainfall estimation with a polarimetric radar in a subtropical environment. *J. Appl. Meteor.,* **41,** 674–685.

Bringi, V. N., and V. Chandrasekar, 2001: *Polarimetric Doppler Weather Radar: Principles and Applications.* Cambridge University Press, 336 pp.

——, ——, N. Balakrishnan, and D. S. Zrnić, 1990: An examination of radar propagation effects in rainfall at microwave frequencies. *J. Atmos. Oceanic Technol.,* **7,** 829–840.

——, T. D. Keenan, and V. Chandrasekar, 2001: Correcting C-band radar reflectivity and differential reflectivity data for rain attenuation: A self-consistent method with constraints. *IEEE Trans. Geosci. Remote Sens.,* **39,** 1906–1915.

——, G.-J. Huang, V. Chandrasekar, and E. Gorgucci, 2002: A methodology for estimating the parameters of a gamma raindrop size distribution model from polarimetric radar data: Application to a squall-line event from the TRMM/Brazil campaign. *J. Atmos. Oceanic Technol.,* **19,** 633–645.

Burgess, D. W., M. A. Magsig, J. Wurman, D. C. Dowell, and Y. Richardson, 2002: Radar observations of the 3 May 1999 Oklahoma City tornado. *Wea. Forecasting,* **17,** 456–471.

Carey, L. D., S. A. Rutledge, D. A. Ahijevych, and T. D. Keenan, 2000: Correcting propagation effects in C-band polarimetric radar observations of tropical convection using differential propagation phase. *J. Appl. Meteor.,* **39,** 1405–1433.

Conway, J. W., and D. S. Zrnić, 1993: A study of embryo production and hail growth using dual-Doppler and multiparameter radars. *Mon. Wea. Rev.,* **121,** 2511–2528.

Doviak, R. J., V. Bringi, A. Ryzhkov, A. Zahrai, and D. Zrnić, 2000: Considerations for polarimetric upgrades to operational WSR-88D radars. *J. Atmos. Oceanic Technol.,* **17,** 257–278.

Dowell, D. C., and H. B. Bluestein, 1997: The Arcadia, Oklahoma, storm of 17 May 1981: Analysis of a supercell during tornadogenesis. *Mon. Wea. Rev.,* **125,** 2562–2582.

Giangrade, S. E., and A. V. Ryzhkov, 2008: Estimation of rainfall based on the results of polarimetric echo classification. *J. Appl. Meteor. Climatol.,* **47,** 2445–2462.

Gourley, J., P. Tabary, and J. Parent du Chatelet, 2007: Empirical estimation of attenuation from differential propagation phase measurements at C band. *J. Appl. Meteor. Climatol.,* **46,** 306–317.

Gu, J.-Y., A. Ryzhkov, P. Zhang, P. Neilley, M. Knight, B. Wolf, and D.-I. Lee, 2011: Polarimetric attenuation correction in heavy rain at C band. *J. Appl. Meteor. Climatol.,* **50,** 39–58.

Herzegh, P. H., and A. R. Jameson, 1992: Observing precipitation through dual-polarization radar measurements. *Bull. Amer. Meteor. Soc.,* **73,** 1365–1374.

Hu, M., and M. Xue, 2007: Impact of configurations of rapid intermittent assimilation of WSR-88D radar data for the 8 May 2003 Oklahoma City tornadic thunderstorm case. *Mon. Wea. Rev.,* **135,** 507–525.

Hubbert, J., V. N. Bringi, and L. D. Carey, 1998: CSU-CHILL polarimetric measurements from a severe hailstorm in eastern Colorado. *J. Appl. Meteor.,* **37,** 749–755.

——, S. M. Ellis, M. Dixon, and G. Meymaris, 2010a: Modeling, error analysis, and evaluation of dual-polarization variables obtained from simultaneous horizontal and vertical polarization transmit radar. Part I: Modeling and antenna errors. *J. Atmos. Oceanic Technol.,* **27,** 1583–1598.

——, ——, ——, and ——, 2010b: Modeling, error analysis, and evaluation of dual-polarization variables obtained from simultaneous horizontal and vertical polarization transmit radar. Part II: Experimental data. *J. Atmos. Oceanic Technol.,* **27,** 1599–1607.

Jang, J.-S. R., 1993: ANFIS: Adaptive-network-based fuzzy inference system. *IEEE Trans. Syst. Man Cybern.,* **23,** 665–685.

Jung, Y., G. Zhang, and M. Xue, 2008a: Assimilation of simulated polarimetric radar data for a convective storm using the ensemble Kalman filter. Part I: Observation operators for reflectivity and polarimetric variables. *Mon. Wea. Rev.,* **136,** 2228–2245.

——, M. Xue, G. Zhang, and J. M. Straka, 2008b: Assimilation of simulated polarimetric radar data for a convective storm using the ensemble Kalman filter. Part II: Parameter estimation experiments. *Mon. Wea. Rev.,* **136,** 2246–2260.

Kumjian, M. R., and A. V. Ryzhkov, 2008: Polarimetric signatures in supercell thunderstorms. *J. Appl. Meteor. Climatol.,* **47,** 1940–1961.

——, and ——, 2009: Storm-relative helicity revealed from polarimetric radar measurements. *J. Atmos. Sci.,* **66,** 667–685.

——, and ——, 2010: The impact of evaporation on polarimetric characteristics of rain: Theoretical model and practical implications. *J. Appl. Meteor. Climatol.,* **49,** 1247–1267.

——, ——, V. M. Melnikov, and T. J. Schuur, 2010: Rapid-scan super-resolution observations of a cyclic supercell with a dual-polarization WSR-88D. *Mon. Wea. Rev.,* **138,** 3762–3786.

Lei, L., G. Zhang, R. D. Palmer, B. L. Cheong, and M. Xue, 2009: A multi-lag correlation estimator for polarimetric radar variables in the presence of noise. Preprints, *34th Conf. on Radar Meteorology,* Williamsburg, VA, Amer. Meteor. Soc., P13.25. [Available online at http://ams.confex.com/ams/pdfpapers/156113.pdf.]

Lemon, L. R., and C. A. Doswell, 1979: Severe thunderstorm evolution and mesocyclone structure as related to tornadogenesis. *Mon. Wea. Rev.,* **107,** 1184–1197.

——, D. W. Burgess, and R. A. Brown, 1978: Tornadic storm airflow and morphology derived from single-Doppler radar measurements. *Mon. Wea. Rev.,* **106,** 48–61.

Loney, M. L., D. S. Zrnić, J. M. Straka, and A. V. Ryzhkov, 2002: Enhanced polarimetric radar signatures above the melting level in a supercell storm. *J. Appl. Meteor.,* **41,** 1179–1194.

MacGorman, D. R., D. W. Burgess, V. Mazur, W. D. Rust, W. L. Taylor, and B. C. Johnson, 1989: Lightning rates relative to tornadic storm evolution on 22 May 1981. *J. Atmos. Sci.,* **46,** 221–251.

Marquis, J., Y. Richardson, J. Wurman, and P. M. Markowski, 2008: Single- and dual-Doppler analysis of a tornadic vortex and surrounding storm-scale flow in the Crowell, Texas, supercell of 30 April 2000. *Mon. Wea. Rev.,* **136,** 5017–5043.

Melnikov, V. M., and D. S. Zrnić, 2007: Autocorrelation and cross-correlation estimators of polarimetric variables. *J. Atmos. Oceanic Technol.,* **24,** 1337–1350.

Palmer, R., and Coauthors, 2009: Weather radar education at the University of Oklahoma—An integrated interdisciplinary approach. *Bull. Amer. Meteor. Soc.,* **90,** 1277–1282.

Park, H. S., A. V. Ryzhkov, D. S. Zrnić, and K.-E. Kim, 2009: The hydrometeor classification algorithm for the polarimetric WSR-88D: Description and application to an MCS. *Wea. Forecasting,* **24,** 730–748.

Payne, C. D., T. J. Schuur, D. R. MacGorman, M. I. Biggerstaff, K. M. Kuhlman, and W. D. Rust, 2010: Polarimetric and electrical characteristics of a lightning ring in a supercell storm. *Mon. Wea. Rev.,* **138,** 2405–2425.

Picca, J. C., and A. V. Ryzhkov, 2010: A multiple-wavelength polarimetric analysis of the 16 May 2010 Oklahoma City hailstorm. Preprints, *25th Conf. on Severe Local Storms,* Denver, CO, Amer. Meteor. Soc., P8.6. [Available online at http://ams.confex.com/ams/pdfpapers/175751.pdf.]

Rasmussen, E. N., 2003: Refined supercell and tornado forecast parameters. *Wea. Forecasting,* **18,** 530–535.

——, and D. O. Blanchard, 1998: A baseline climatology of sounding-derived supercell and tornado forecast parameters. *Wea. Forecasting,* **13,** 1148–1164.

Romine, G. S., D. W. Burgess, and R. B. Wilhelmson, 2008: A dual-polarization-radar-based assessment of the 8 May 2003 Oklahoma City tornado supercell. *Mon. Wea. Rev.,* **136,** 2849–2870.

Ryzhkov, A. V., and D. S. Zrnić, 2007: Depolarization in ice crystals and its effect on radar polarimetric measurements. *J. Atmos. Oceanic Technol.,* **24,** 1215–1230.

——, D. Burgess, D. Zrnić, T. Smith, and S. Giangrande, 2002: Polarimetric analysis of a 3 May 1999 tornado. Preprints, *21st Conf. on Severe Local Storms,* Hyannis, MA, Amer. Meteor. Soc., 14.2. [Available online at http://ams.confex.com/ams/pdfpapers/47348.pdf.]

——, S. E. Giangrande, and T. J. Schuur, 2005a: Rainfall estimation with a polarimetric prototype of WSR-88D. *J. Appl. Meteor.,* **44,** 502–515.

——, T. J. Schuur, D. W. Burgess, P. L. Heinselman, S. E. Giangrande, and D. S. Zrnić, 2005b: The Joint Polarization Experiment: Polarimetric rainfall measurements and hydrometeor classification. *Bull. Amer. Meteor. Soc.,* **86,** 809–824.

——, ——, ——, and D. S. Zrnić, 2005c: Polarimetric tornado detection. *J. Appl. Meteor.,* **44**, 557–570.

——, S. Ganson, A. Khain, M. Pinsky, and A. Pokrovsky, 2009: Polarimetric characteristics of melting hail at S and C bands. Preprints, *34th Conf. on Radar Meteorology,* Williamsburg, VA, Amer. Meteor. Soc., 4A.6. [Available online at http://ams.confex.com/ams/pdfpapers/155571.pdf.]

Seliga, T. A., and V. N. Bringi, 1976: Potential use of radar differential reflectivity measurements at orthogonal polarizations for measuring precipitation. *J. Appl. Meteor.,* **15,** 69–76.

Snyder, J. C., H. B. Bluestein, G. Zhang, and S. J. Frasier, 2010: Attenuation correction and hydrometeor classification of high-resolution, X-band, dual-polarized mobile radar measurements in severe convective storms. *J. Atmos. Oceanic Technol.,* **27,** 1979–2001.

Speheger, D. A., C. A. Doswell, and G. J. Stumpf, 2002: The tornadoes of 3 May 1999: Event verification in central Oklahoma and related issues. *Wea. Forecasting,* **17,** 362–381.

Straka, J. M., E. N. Rasmussen, and S. E. Fredrickson, 1996: A mobile Mesonet for finescale meteorological observations. *J. Atmos. Oceanic Technol.,* **13,** 921–936.

——, D. S. Zrnić, and A. V. Ryzhkov, 2000: Bulk hydrometeor classification and quantification using polarimetric radar data: Synthesis of relations. *J. Appl. Meteor.,* **39,** 1341–1372.

Sugeno, M., 1985: *Industrial Applications of Fuzzy Control.* Elsevier, 278 pp.

Tabary, P., G. Vulpiani, J. Gourley, A. Illingworth, R. Thompson, and O. Bousquet, 2009: Unusually high differential attenuation at C band: Results from a two-year analysis of the French Trappes polarimetric radar data. *J. Appl. Meteor. Climatol.,* **48,** 2037–2053.

Testud, J., E. Le Bouar, E. Obligis, and M. Ali-Mehenni, 2000: The rain profiling algorithm applied to polarimetric weather radar. *J. Atmos. Oceanic Technol.,* **17,** 332–456.

Thompson, R. L., R. Edwards, J. A. Hart, K. L. Elmore, and P. Markowski, 2003: Close proximity soundings within supercell environments obtained from the Rapid Update Cycle. *Wea. Forecasting,* **18,** 1243–1261.

——, C. M. Mead, and R. Edwards, 2007: Effective storm-relative helicity and bulk shear in supercell thunderstorm environments. *Wea. Forecasting,* **22,** 102–115.

Vivekanandan, J., S. M. Ellis, R. Oye, D. S. Zrnic, A. V. Ryzhkov, and J. Straka, 1999: Cloud microphysics retrieval using S-band dual-polarization radar measurements. *Bull. Amer. Meteor. Soc.,* **80,** 381–388.

Vulpiani, G., P. Tabary, J. Parent du Chatelet, and F. Marzano, 2008: Comparison of advanced radar polarimetric techniques for operational attenuation correction at C band. *J. Atmos. Oceanic Technol.,* **25,** 1118–1135.

Wakimoto, R. M., W.-C. Lee, H. B. Bluestein, C.-H. Liu, and P. H. Hildebrand, 1996: ELDORA observations during VORTEX 95. *Bull. Amer. Meteor. Soc.,* **77,** 1465–1481.

Wang, Y., and T.-Y. Yu, 2009: Advanced tornado detection algorithm using super-resolution and polarimetric data. Preprints, *34th Conf. on Radar Meteorology,* Williamsburg, VA, Amer. Meteor. Soc, P5.14. [Available online at http://ams.confex.com/ams/pdfpapers/155969.pdf.]

——, ——, M. Yeary, A. Shapiro, N. Shamim, M. Foster, D. Andra, and M. Jain, 2008: Tornado detection using a neuro-fuzzy system to integrate shear and spectral signatures. *J. Atmos. Oceanic Technol.,* **25,** 1136–1148.

Warde, D., and S. Torres, 2010: A novel ground-clutter-contamination mitigation solution for the NEXRAD network: The CLEAN-AP filter. Preprints, *26th Conf. on Interactive Information and Processing Systems (IIPS) for Meteorology, Oceanography, and Hydrology,* Atlanta, GA, Amer. Meteor. Soc., 8.6.[Available online at http://ams.confex.com/ams/90annual/techprogram/paper-163834.htm.]

Weisman, M. L., and J. B. Klemp, 1982: The dependence of numerically simulated convective storms on vertical wind shear and buoyancy. *Mon. Wea. Rev.,* **110,** 504–520.

Wurman, J., and M. Randall, 2001: An inexpensive, mobile, rapid-scan radar. Preprints, *30th Int. Conf. on Radar Meteorology,* Munich, Germany, Amer. Meteor. Soc., 98–100.

——, J. Straka, E. Rasmussen, M. Randall, and A. Zahrai, 1997: Design and deployment of a portable, pencil-beam, pulsed, 3-cm Doppler radar. *J. Atmos. Oceanic Technol.,* **14,** 1502–1512.

Yeary, M., S. Nemati, T.-Y. Yu, and Y. Wang, 2007: Tornadic time series detection using eigen analysis and a machine intelligence-based approach. *IEEE Trans. Geosci. Remote Sens.,* **4,** 335–339.

Yu, T.-Y., Y. Wang, A. Shapiro, M. Yeary, D. S. Zrnić and R. J. Doviak, 2007: Characterization of tornado spectral signatures using higher order spectra. *J. Atmos. Oceanic Technol.,* **24,** 1997–2013.

Zhang, G., J. Vivekanandan, and E. Brandes, 2001: A method for estimating rain rate and drop size distribution form polarimetric radar measurements. *IEEE Trans. Geosci. Remote Sens.,* **39,** 831–841.

——, R. J. Doviak, J. Vivekanandan, W. O. J. Brown, and S. A. Cohn, 2004: Performance of correlation estimators for spaced-antenna wind measurement in the presence of noise. *Radio Sci.,* **39,** RS3017, doi:10.1029/2003RS003022.

——, ——, D. S. Zrnić, J. Crain, D. Stainman, and Y. Al-Rashid, 2009: Phased array radar polarimetry for weather sensing: A theoretical formulation for bias correction. *IEEE Trans. Geosci. Remote Sens.,* **47,** 3679–3689.

Zrnić, D. S., 1996: Simultaneous differential polarimetric measurements and co-polar correlation coefficient measurement. U.S. Patent 5500646, 7 pp.

——, and R. J. Doviak, 1975: Velocity spectra of vortices scanned with a pulsed-Doppler radar. *J. Appl. Meteor.,* **14,** 1531–1539.

——, and A. V. Ryzhkov, 1999: Polarimetry for weather surveillance radars. *Bull. Amer. Meteor. Soc.,* **80,** 389–346.

——, D. W. Burgess, and L. Hennington, 1985: Doppler spectra and estimated windspeed of a violent tornado. *J. Climate Appl. Meteor.,* **24,** 1068–1081.

——, R. J. Doviak, G. Zhang, and A. V. Ryzhkov, 2010: Bias in differential reflectivity due to cross coupling through the radiation patterns of polarimetric weather radars. *J. Atmos. Oceanic Technol.,* **27,** 1624–1637.